

Optimal Dirichlet Boundary Control by Fourier Neural Operators Applied to Nonlinear Optics

Nils Margenberg ^{*†} Franz X. Kärtner ^{‡§} Markus Bause ^{*}

We present an approach for solving optimal Dirichlet boundary control problems of nonlinear optics by using deep learning. For computing high resolution approximations of the solution to the nonlinear wave model, we propose higher order space-time finite element methods in combination with collocation techniques. Thereby, C^l -regularity in time of the global discrete is ensured. The resulting simulation data is used to train solution operators that effectively leverage the higher regularity of the training data. The solution operator is represented by Fourier Neural Operators and Gated Recurrent Units and can be used as the forward solver in the optimal Dirichlet boundary control problem.

The proposed algorithm is implemented and tested on modern high-performance computing platforms, with a focus on efficiency and scalability. The effectiveness of the approach is demonstrated on the problem of generating Terahertz radiation in periodically poled Lithium Niobate, where the neural network is used as the solver in the optimal control setting to optimize the parametrization of the optical input pulse and maximize the yield of 0.3 THz-frequency radiation.

We exploit the periodic layering of the crystal to design the neural networks. The networks are trained to learn the propagation through one period of the layers. The recursive application of the network onto itself yields an approximation to the full problem. Our results indicate that the proposed method can achieve a significant speedup in computation time compared to classical methods. A comparison of our results to experimental data shows the potential to revolutionize the way we approach optimization problems in nonlinear optics.

MSC2020: 78M50, 78M10, 78A60, 65M60, 49M41

Keywords: Optimal Control, Neural Operators, Deep Neural Networks, Nonlinear Optics, Space-Time Finite Element Method

1. Introduction

1.1. Physical Problem and Machine Learning approach

Nonlinear optical phenomena play a fundamental role in a lot of applications, including the development of innovative optical sources. As high-intensity lasers become more accessible and complexity increases, the simulation of nonlinear optical phenomena gains importance in order to achieve optimal performance and reduce the cost and time for empirical studies.

In this work we are concerned with the generation of Terahertz (THz) radiation, which spans the frequency range of 0.1 THz to 30 THz. Thus, it is positioned between the microwave and infrared

^{*}Helmut Schmidt University, Faculty of Mechanical and Civil Engineering, Holstenhofweg 85, 22043 Hamburg, Germany

[†]Corresponding author: margenbn@hsu-hh.de

[‡]Center for Free Electron Laser Science (CFEL), Deutsches Elektronen-Synchrotron (DESY) & Department of Physics, University of Hamburg, Notkestraße 85, 22607 Hamburg, Germany

[§]The Hamburg Center for Ultrafast Imaging, Luruper Chaussee 149, 22761 Hamburg, Germany

electromagnetic frequency bands. THz radiation offers great potential for a wide range of ultrafast spectroscopic, strong field and imaging applications. However, a persistent challenge in current research lies in the limited availability of compact THz sources capable of delivering both high field strength and high repetition rates. We address this limitation through the development of machine learning techniques to elucidate and optimize THz generation in nonlinear crystals. By leveraging these approaches, we aim to pave the way for the next generation of compact and efficient light sources for spectroscopic applications, thereby enabling significant advancements in the field [46].

In this paper, we develop machine learning techniques to solve an optimal control problem that arises in the optimization of THz radiation generation in nonlinear crystals. Specifically, the problem can be formulated as an optimal Dirichlet boundary control problem, which requires the repeated solution of the forward problem. While we previously developed accurate simulation methods for a class of nonlinear dispersive wave equations in nonlinear optics [65], each simulation entails a significant computational effort. Consequently, the solution of the forward problem with this method is impractical for the integration into the optimal control problem, which necessitates different approaches.

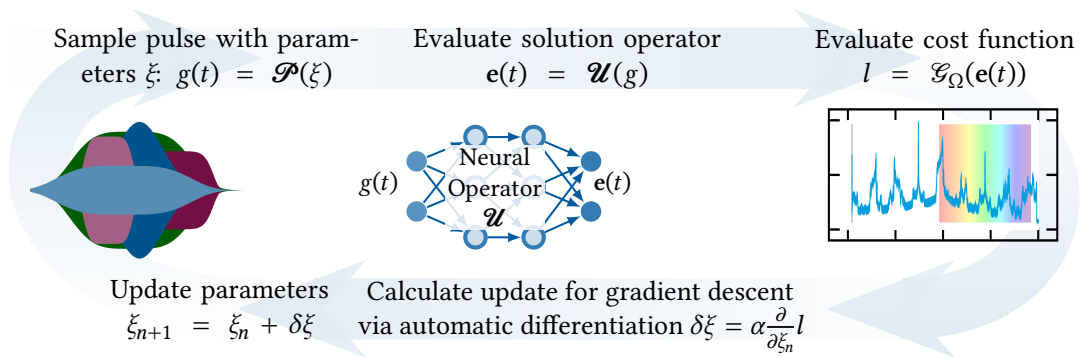


Figure 1: Sketch of the algorithm presented in this paper. We use a differentiable sampler, which generates the controls and a Neural Operator which solves the forward problem. The parametrization of the control is then optimized with a gradient descent method. The graph on the right shows the spectrum of the electric field. Here the goal is to maximize the 0.3 THz-frequency radiation, marked by the small bar at the left.

The key ideas of our method are sketched in Fig. 1. The first aspect of the method we develop is the differentiability of a program that is implemented using established Artificial Neural Network (ANN) libraries. This paradigm is known as differentiable programming [77].

The second main idea in our algorithm builds on the periodicity of the material parameters. We consider a problem in nonlinear optics which involves a periodically poled nonlinear crystal. We learn a solution operator U to the forward problem in a single period of the crystal. By recursive application of U onto itself we approximate the solution operator for multiple layers. The resulting solution operator can then be integrated into the solution of an optimal control problem.

In our work, we adopt a hybrid approach that combines classical and mature numerical methods, specifically finite element methods, with deep learning techniques. We use numerical methods where they have clear advantages over machine learning approaches, while we use ANNs where numerical methods are not feasible or efficient. Our approach to solving an optimal Dirichlet boundary control problem exemplifies this paradigm, which is the focus of this work. In particular, we extend our previous work [65] on space-time finite element methods by using higher order variational time discretizations presented in [2, 4]. The resulting finite element solution has global C^1 -regularity in time. We then use the resulting simulation data to train a solution operator that effectively leverages

the higher regularity of the training data. The numerical and machine learning methods are implemented and tested on modern high-performance computing platforms, with a focus on efficiency and scalability.

1.2. Related works

Partial differential equations (PDEs) play a fundamental role in science and engineering. They describe natural phenomena and processes in a lot of scientific fields and provide a mathematical framework to model these phenomena. Despite the significant advances in recent decades, challenges persist, e. g. in the context of addressing the solution of large-scale systems of nonlinear equations.

Machine Learning for partial differential equations

Approaches for the solution of PDEs using ANNs trace back more than 20 years, e. g. [54]. The idea is to directly parametrize the solution to the PDE as an ANN. The network is then trained by incorporating the differential equation, along with the boundary conditions, into the loss function. In [28] Weinan and Yu minimize an energy functional, resembling the variational formulation used in FEM. On the other hand, DeepXDE [63], PINN [78], and the Deep Galerkin Method [82] use different approaches where the strong residual of the PDE is minimized. This is done through collocation methods on randomly selected points within the domain and on the boundary. Karniadakis and Zhang proposed VPINNs [48], where the cost function is the variational formulation, which is optimized by sampling test functions. A comprehensive review of PINN and related approaches in the field of Scientific Machine Learning can be found in [22]. The authors of [20, 40, 45, 66] develop ANNs that ensure the symplectic structure of Hamiltonian mechanics, which improves generalization and accuracy. Based on Koopmann operator representation, the authors of [34, 74] train an ANN to represent a coordinate transformation that linearizes a nonlinear PDE.

A recent approach to solving PDEs involves learning solution operators using artificial neural networks. This technique involves approximating solution operators using ANNs, which can potentially enable the solution of complex problems. A significant advantage of this approach is that once the solution operator is trained, it can be applied to other scenarios. Training ANNs is computationally expensive, which makes PINNs and related approaches not competitive to classical simulation methods [37]. Evaluating an ANN on the other hand is computationally cheap, making neural operators appealing: Once a solution operator is trained, it can be generalized to other scenarios, which only requires the evaluation of the network. Various architectures exist for constructing these neural operators. In [62], Lu et al. construct an architecture called DeepONets by iterating a shallow network proposed in [19]. This type of network consists of a trunk network which is applied to an input function and a branch net which is applied to an element from the domain of the operator. In [56] the authors prove an error estimate for the DeepONet architecture. Other approaches to learn solution operators are inspired by reduced basis methods [14, 33, 69, 71, 73, 80]. Based on low rank decompositions the authors of [49] introduce an ANN with low-rank structure to approximate the inverse of differential operators. In [53], the authors construct such a network as the tensor product of two networks, which also carries similarities with the DeepONet architecture [61].

Building on [30, 31, 47], the Fourier Neural Operator (FNO) architecture are developed in [53, 57]. In [52] the authors prove a universal approximation property and error bounds. Based on FNOs, new architectures are developed, e. g. Neural Inverse Operators [68] which are used to solve inverse problems.

The idea of designing and interpreting ANNs using continuity becomes increasingly popular. A

notable example of this is the formulation of ResNet as a continuous time process with respect to the depth parameter [26, 39]. See also [5] for an extension to adaptive timestepping, where the timestep-size is a parameter, which can be optimized. Similarly, works linking ANNs and dynamical systems observe that problems arising in deep learning can be recast into optimal control problems on differential equations [11, 27, 44, 60, 81]. Recent works employ deep learning techniques to address computational challenges encountered in solving optimal control problems; The works [12, 84] and references therein serve as a good basis for a comprehensive survey. Existing work is mainly concerned with stochastic control [17, 18, 79]. This is in contrast to this work, where we are concerned with Dirichlet optimal control problems.

Space-Time Finite Element Methods

We describe the numerical simulations of nonlinear optical phenomena in the context of space-time finite element methods [51]. Specifically we use time discretization of higher order and regularity [2, 4]. Other investigations on space-time finite element methods were conducted in [24, 25], where numerical results with an adaptive algorithm are presented. Further work relevant for electromagnetic problems is the PhD thesis [32] and references therein. Various alternative methods for discretizing wave equations via space-time finite element methods exist, and they are discussed in depth in [55]. Notable examples include the works of [8, 35], as well as more recent developments such as those presented in [76, 83]. These works and their references serve as a good basis for a comprehensive survey of recent developments in space-time discretization techniques for linear wave equations.

The advantages of the variational time discretization include the natural integration with the variational discretization in space and that it naturally captures couplings and nonlinearities. These features facilitate the use of concepts such as duality and goal oriented adaptivity [9]. The concepts of variational space-time discretization also offers a unified approach to stability and error analysis as shown in [67]. Furthermore, the use of space-time FEM allow us to solve the wave equation together with the arising ADEs in one holistic framework [65]. Once the formulation is established, the methods can be extended in a generic manner. For instance, we introduced the physical problem we are concerned with in this work in [65] and extend it here to the family of Galerkin-collocation methods [4].

2. Notation and Mathematical Problem

Let $\mathcal{D} \subset \mathbb{R}^d$ with $d \in \{1, 2, 3\}$ be a bounded domain with boundary $\partial\mathcal{D} = \Gamma_D$ and $I = (0, T]$ a bounded time interval with final time $T > 0$. By $H^m(\mathcal{D})$ we denote the Sobolev space of $L^2(\mathcal{D})$ functions with derivatives up to order m in $L^2(\mathcal{D})$. For the definition of these function spaces we refer to [29]. We let $L := L^2(\mathcal{D})$, $V = H^1(\mathcal{D})$ and $V_0 = H_0^1(\mathcal{D})$ be the space of all H^1 -functions with vanishing trace on the Dirichlet part of the boundary Γ_D . We denote the L^2 -inner product by $\langle \cdot, \cdot \rangle$. For the norms we use $\|\cdot\| := \|\cdot\|_{L^2(\mathcal{D})}$ and $\|\cdot\|_m := \|\cdot\|_{H^m(\mathcal{D})}$ for $m \in \mathbb{N}$ and $m \geq 1$. By $L^2(0, T; B)$, $C([0, T]; B)$ and $C^q([0, T]; B)$, for $q \in \mathbb{N}$, we denote the standard Bochner spaces of B -valued functions for a Banach space B , equipped with their natural norms. Further, for a subinterval $J \subseteq [0, T]$, we will use the notations $L^2(J; B)$, $C^m(J; B)$ and $C^0(J; B) := C(J; B)$ for the corresponding Bochner spaces. Further, we define the function spaces, that we need below for the variational formulation of the model equations.

Definition 2.1: Function spaces for the variational formulations

$$W(I) = \{ \mathbf{w} \in L^2(I; V) \mid \partial_t \mathbf{w} \in L^2(I; L) \}, \quad (2.1a)$$

$$W_0(I) = \{ \mathbf{w} \in L^2(I; V_0) \mid \partial_t \mathbf{w} \in L^2(I; L) \}, \quad (2.1b)$$

$$W_{\text{nl}}(I) = \{ \mathbf{w} \in L^2(I; V) \mid \partial_t \mathbf{w} \in L^2(I; L), \partial_t(|\mathbf{w}| \mathbf{w}) \in L^2(I; L) \}. \quad (2.1c)$$

In (2.1c) we denote by $|\mathbf{w}|$ the contraction of \mathbf{w} , i.e. $|\mathbf{w}| = \sum_{i=1}^d w_i$.

Mathematical model problem from nonlinear optics

In this work we study nonlinear dispersive wave propagation, that is modeled by the following coupled partial differential equation (cf. [1, 65]). Its physical background and application is discussed further in Section 2.1.

Problem 2.1: Nonlinear dispersive wave equation

$$\partial_{tt} \mathbf{p} + \Gamma_0 \partial_t \mathbf{p} + \nu_t^2 \mathbf{p} - (\varepsilon_\Omega - \varepsilon_\omega) \nu_t^2 \mathbf{e} = 0 \quad \text{on } \mathcal{D} \times I, \quad (2.2a)$$

$$-\Delta \mathbf{e} + \varepsilon_\omega \partial_{tt} \mathbf{e} + (\varepsilon_\Omega - \varepsilon_\omega) \nu_t^2 \mathbf{e} - \nu_t^2 \mathbf{p} - \Gamma_0 \partial_t \mathbf{p} + \chi^{(2)} \partial_{tt}(|\mathbf{e}| \mathbf{e}) = \mathbf{f} \quad \text{on } \mathcal{D} \times I, \quad (2.2b)$$

$$\mathbf{e}(0) = \mathbf{e}_0, \quad \partial_t \mathbf{e}(0) = \mathbf{e}_1, \quad \mathbf{p}(0) = \mathbf{p}_0, \quad \partial_t \mathbf{p}(0) = \mathbf{p}_1 \quad \text{on } \mathcal{D}, \quad (2.2c)$$

$$\mathbf{e} = \mathbf{g}^e \quad \text{on } \Gamma_D. \quad (2.2d)$$

By \mathbf{e} we denote the electric field, by \mathbf{p} the polarization and $\Gamma_0, \nu_t, \varepsilon_\omega, \varepsilon_\Omega \in \mathbb{R}_+$ are material parameters. We further define $\varepsilon_\Delta = \varepsilon_\Omega - \varepsilon_\omega$. The boundary condition \mathbf{g}^e is a prescribed trace on Γ_D and \mathbf{f} is an external force acting on the domain. To simplify the notation and enable better numerical treatment lateron, we have already expressed Problem 2.1 in normalized quantities. Specifically, we have transformed the equations and quantities using the transformation $\tilde{t} = c_0 t$, where c_0 is the speed of light in vacuum. This normalization is consistently applied throughout this work. Therefore, we omit the tilde notation, as we already did in (2.2). For the numerical approximation we reformulate Problem 2.1 as a first-order system in time; cf. Problem 2.2. To this end we introduce the auxiliary variables

$$\mathbf{u} = \partial_t \mathbf{p} + \Gamma_0 \mathbf{p}, \quad (2.3a) \quad \mathbf{a} = \varepsilon_\omega \partial_t \mathbf{e} - \Gamma_0 \mathbf{p} + \chi^{(2)} \partial_t(|\mathbf{e}| \mathbf{e}). \quad (2.3b)$$

We tacitly assume that Problem 2.1 has a sufficiently regular, unique solution. The proof of existence and uniqueness for the nonlinear system (2.2) extends beyond the scope of this work. However, it is crucial for our subsequent mathematical arguments and formulations that the solution to Problem 2.1 is regular enough such that all the mathematical arguments and formulations used below are well-defined and the application of higher order discretization techniques becomes reasonable. This regularity, in turn, imposes certain conditions on the data, coefficients, and geometric properties of the domain; cf. [29]. Under the assumption of the existence of a unique and smooth solution to (2.2), this solution satisfies the following weak formulation.

Problem 2.2: Weak formulation of the nonlinear dispersive wave equation (2.2)

For given data $\mathbf{f} \in L^2(I; L)$, boundary conditions $g^e \in L^2(I; H^{1/2}(\Gamma_D))$ and initial conditions $(\mathbf{u}_0, \mathbf{p}_0, \mathbf{a}_0, \mathbf{e}_0) =: \mathbf{v}_0 \in L^3 \times V$ find $\mathbf{v} := (\mathbf{u}, \mathbf{p}, \mathbf{a}, \mathbf{e}) \in (W(I), W(I), W(I), W_{\text{nl}}(I)) =: \mathbf{W}(I)$ such that $\mathbf{e}|_{\Gamma_D} = g^e$ and for all $\Phi \in (W_0(I))^4$

$$\mathcal{A}(\mathbf{v})(\Phi) = \mathbf{F}(\Phi) \quad (2.4)$$

is satisfied. The functional $\mathbf{F} : (W_0(I))^4 \rightarrow \mathbb{R}$ and the semilinear form, which is linear in the second argument, $\mathcal{A} : \mathbf{W}(I) \times (W_0(I))^4 \rightarrow \mathbb{R}$ are given by

$$\begin{aligned} \mathcal{A}(\mathbf{v})(\Phi) := & \int_0^T \langle \partial_t \mathbf{p}, \phi^0 \rangle + \Gamma_0 \langle \mathbf{p}, \phi^0 \rangle - \langle \mathbf{u}, \phi^0 \rangle dt + \langle \mathbf{u}(0), \phi^0(0) \rangle \\ & + \int_0^T v_t^2 \langle \mathbf{p}, \phi^1 \rangle - \varepsilon_\Delta v_t^2 \langle \mathbf{e}, \phi^1 \rangle + \langle \partial_t \mathbf{u}, \phi^1 \rangle dt + \langle \mathbf{p}(0), \phi^1(0) \rangle \\ & + \int_0^T \varepsilon_\omega \langle \partial_t \mathbf{e}, \phi^2 \rangle - \Gamma_0 \langle \mathbf{p}, \phi^2 \rangle + \chi^{(2)} \langle \partial_t (|\mathbf{e}| \mathbf{e}), \phi^2 \rangle - \langle \mathbf{a}, \phi^2 \rangle dt + \langle \mathbf{a}(0), \phi^2(0) \rangle \\ & + \int_0^T \langle \nabla \mathbf{e}, \nabla \phi^3 \rangle + \varepsilon_\Delta v_t^2 \langle \mathbf{e}, \phi^3 \rangle - v_t^2 \langle \mathbf{p}, \phi^3 \rangle + \langle \partial_t \mathbf{a}, \phi^3 \rangle dt + \langle \mathbf{e}(0), \phi^3(0) \rangle, \end{aligned} \quad (2.5a)$$

$$\mathbf{F}(\phi) := \langle \mathbf{u}_0, \phi^0(0) \rangle + \langle \mathbf{p}_0, \phi^1(0) \rangle + \langle \mathbf{a}_0, \phi^2(0) \rangle + \langle \mathbf{e}_0, \phi^3(0) \rangle + \int_0^T \langle \mathbf{f}, \phi^3 \rangle dt. \quad (2.5b)$$

We note that all integrals in (2.4) are well-defined in the function space $\mathbf{W}(I)$, due to the Definition 2.1. To obtain higher regularity of the solution, stricter assumptions \mathbf{f} and \mathbf{v}_0 may have to be imposed.

Remark 2.1: Weakly imposed initial conditions

In (2.5), the expressions $\mathbf{w}(0)$ for $\mathbf{w} \in \{\mathbf{u}, \mathbf{p}, \mathbf{a}, \mathbf{e}\}$ are well-defined when we consider the continuous embedding $W \hookrightarrow C(\bar{I}; V)$, cf. [23, Chapter XVIII, Theorem 1]. We further note that the test space W_0 is dense in $L^2(I; V_0)$, as stated in [16, Chapter 2, Corollary 2.1].

Based on Remark 2.1, we comment on the variational problem (2.4).

- For convenience, the initial conditions of Problem 2.2 are incorporated in the variational equation (2.4) through the forms (2.5). The Sobolev embedding $\mathbf{W}(I) \hookrightarrow C(\bar{I}; V)^4$ ensures the well-defined pointwise evaluation of functions in $\mathbf{W}(I)$ within the forms (2.5).
- According to Remark 2.1, the test space $W_0(I)^4$ is densely embedded in the Hilbert space $L^2(I; V_0)^4$. This dense embedding is an indispensable requirement for the proper formulation of Problem 2.2.
- The variables $(\mathbf{u}, \mathbf{p}, \mathbf{a}, \mathbf{e})$ belong to the solution space $\mathbf{W}(I)$. Although weaker assumptions about \mathbf{u} , \mathbf{p} and \mathbf{a} would have been sufficient for the existence of the space-time integrals in (2.4). However, we adopt this stronger assumption since we use an $H^1(\mathcal{D})$ -conforming approximation for all variables in Section 3. This concept follows the lines of [7].

Under the above-made assumptions we now define the solution operator that is associated with Problem 2.2 and its weak formulation (2.4).

Definition 2.2: Solution Operator

Consider the nonlinear Problem 2.2. The solution operator

$$\begin{aligned} \mathcal{S} : D(\mathcal{S}) \subset L^2(I; H^{1/2}(\Gamma_D)) \times L^2(I; L) \times (L^3 \times V) &\rightarrow \mathbf{W}(I), \\ (g^e, \mathbf{f}, \mathbf{v}_0) &\mapsto \mathbf{v}. \end{aligned} \quad (2.6)$$

is defined by the mapping of the data \mathbf{f} and the initial conditions \mathbf{v}_0 to the unique solution \mathbf{v} of (2.4), such that

$$\mathcal{A}(\mathcal{S}(g^e, \mathbf{f}, \mathbf{v}_0))(\Phi) = \mathbf{F}(\Phi) \quad \forall \Phi \in (W_0(I))^4. \quad (2.7)$$

The domain $D(\mathcal{S})$ is supposed to be a subset of sufficiently regular functions \mathbf{f}, \mathbf{v}_0 in $L^2(I; H^{1/2}(\Gamma_D)) \times L^2(I; L) \times (L^3 \times V)$ such that (2.7) admits a unique solution with the regularity required for the numerical approximation scheme. The goal of this work is to approximate the operator \mathcal{S} by an ANN, which evaluation involves low computational costs and thereby lets an optimal control problem subject to the Dirichlet data of Problem 2.2 become feasible. For the training and validation of the ANN approximate solutions to Problem 2.2 with high resolution are necessary. They are computed by space-time finite element techniques of high accuracy which are presented in Section 3.

2.1. Physical Background

Based on [65], we review the model (2.2), with a focus on the applications and physics of nonlinear optics [15, 70]. Nonlinear and dispersive effects arise due to the interaction of waves with atoms or molecules in a medium. The polarization \mathbf{p} of the medium captures these interactions at a macroscopic level. The polarization can be developed as a power series in terms of the electric field \mathbf{e} . Based on the physical settings and materials considered in this work, it is deemed sufficient to include only the linear and quadratic terms to accurately model the phenomena of interest. The polarization is then given by

$$\mathbf{p}(x, t) = \varepsilon_0 \left(\chi^{(1)} \otimes \mathbf{e}(x, t) + \chi^{(2)} \otimes \mathbf{e}(x, t) \otimes \mathbf{e}(x, t) \right),$$

where the electric susceptibilities $\chi^{(n)} : \mathbb{R} \times \mathcal{D} \rightarrow \otimes_{i=0}^n \mathbb{C}^d$ are tensor-valued functions which depend on the frequency and spatial coordinate. We assume that $\chi^{(1)}$ and $\chi^{(2)}$ can be simplified to scalar functions such that

$$\chi^{(1)} : \mathbb{R} \rightarrow \mathbb{C} \quad \text{and} \quad \chi^{(2)} : \mathcal{D} \rightarrow \mathbb{R}. \quad (2.8)$$

We note that $\chi^{(1)}$ doesn't depend on spatial coordinates and the material is homogeneous w. r. t. to the linear susceptibility. Further, we only consider instantaneous nonlinearities, which means that the nonlinear susceptibilities are frequency independent. We formulate the dispersive electromagnetic wave equation

$$-\Delta \mathbf{e} + \partial_{tt} \varepsilon_r * \mathbf{e} + \chi^{(2)} \partial_{tt} (|\mathbf{e}| \mathbf{e}) = \mathbf{f}. \quad (2.9)$$

Here ε_r is the relative electric permittivity for which $\varepsilon_r = n^2 = 1 + \chi^{(1)}$ holds, where n is the refractive index. A simple model introduced by Lorentz, which describes the electric permittivity ε_r as a function of the frequency ν is given by

$$\varepsilon_r(\nu) = \varepsilon_\omega + \frac{(\varepsilon_\Omega - \varepsilon_\omega) \nu_t^2}{\nu_t^2 - \nu^2 + i\Gamma_0 \nu}. \quad (2.10)$$

The physical model for (2.10) is an electron bound to the nucleus by a force governed by Hooke's law with characteristic frequency ν_t . Γ_0 is the damping coefficient and ε_Ω and ε_ω are the low and high frequency limits of the relative electric permittivity. In the time domain (2.10) gives rise to the

convolution term $[\varepsilon_r(v) * \mathbf{e}](t)$ in (2.9). To avoid the computationally expensive evaluation of this convolution, we derive an auxiliary differential equation (ADE), as given by (2.2a). By substituting (2.2a) into (2.9), we obtain (2.2b), which results in the formulation of Problem 2.1.

3. Variational Space-Time Discretization for Nonlinear Dispersive Wave Equations

In this section we present the numerical approximation scheme that we use for highly resolved and accurate computations of solutions to the weak form (2.4) of the nonlinear dispersive wave problem in Problem 2.1.

The approach discretizes the continuous system (2.2) by enforcing differentiability in time constraints on the trial space of piecewise polynomials in combination with variational conditions, based on the weak formulation (2.4) and collocation conditions, deduced from the strong form (2.2). The collocation conditions are imposed at the end point of the subintervals of the time mesh. Due to the differentiability in time, we will observe that the collocation conditions are also satisfied at the initial time points of the subintervals. These schemes are referred to as Galerkin-collocation methods, for short GCC^s(k) where s denotes the differentiability with respect to the time variable and k the order of the polynomials of the trial space. Galerkin-collocation schemes have been introduced and studied for acoustic waves in [2, 4]. For the choice $r = k$ (r being the order of approximation in space), convergence of order $k + 1$ in space and time is shown for the fully discrete approximation of the solution and its time derivative. In our simulations presented in Section 6 we put $k = 3$. In the numerical investigations of Section 6, we will see that Galerkin-collocation are strongly adapted to the accurate and efficient numerical simulation of nonlinear dispersive phenomena.

The collocation conditions allow us to reduce the size of the discrete variational test space, which leads to increased efficiency compared to standard Galerkin-Petrov approaches, as presented in [51] for example. Galerkin-collocation schemes lead to discrete solutions of higher order regularity in time. For instance, by employing the GCC¹(3) method, the simplest scheme from this family of time discretization techniques, we obtain solutions of C^1 -regularity in time, which is particularly advantageous for wave problems. We also exploit the increased regularity in our optimal control method by neural networks in Section 5.

For the time discretization, we split the time interval I into a sequence of N disjoint subintervals $I_n = (t_{n-1}, t_n]$, $n = 1, \dots, N$. For a Banach space B and $k \in \mathbb{N}_0$ we define

$$\mathbb{P}_k(I_n; B) = \left\{ w_{\tau_n} : I_n \rightarrow B \mid w_{\tau_n}(t) = \sum_{j=0}^k W^j t^j \quad \forall t \in I_n, W^j \in B \quad \forall j \right\}. \quad (3.1)$$

For $r \in \mathbb{N}$ we define the finite element space that is built on the spatial mesh as

$$\mathcal{V}_h = \left\{ v_h \in C(\bar{D}) \mid v_h|_K \in \mathcal{Q}_r(K) \quad \forall K \in \mathcal{T}_h \right\}, \quad \mathcal{V}_{h,0} = \mathcal{V}_h \cap V_0, \quad (3.2)$$

where $\mathcal{Q}_r(K)$ is the space defined by the reference mapping of polynomials on the reference element with maximum degree r in each variable. From now on we choose the piecewise polynomial degrees in (3.1) and (3.2) to $k = 3$ and $r = 3$. The trial and test space for our discrete problem are then defined by

$$\begin{aligned} X_{\tau,h} &= \left\{ w \in C^1(\bar{I}; \mathcal{V}_h) \mid w|_{I_n} \in \mathbb{P}_3(I_n; \mathcal{V}_h) \quad \forall n = 1, \dots, N \right\}, \\ Y_{\tau,h} &= \left\{ w \in L^2(I; \mathcal{V}_{h,0}) \mid w|_{I_n} \in \mathbb{P}_0(I_n; \mathcal{V}_{h,0}) \quad \forall n = 1, \dots, N \right\}. \end{aligned} \quad (3.3)$$

We impose global C^1 -regularity on $X_{\tau,h}$, which corresponds to a spline-type discretization in time. We chose the global time-discrete space of piecewise constant functions as $Y_{\tau,h}$. Thereby, we need to fix additional degrees of freedom in order to ensure solvability. To this end, we combine the C^1 -regularity constraints with the strong form of the equations at the endpoints of each subinterval I_n . Then, collocation conditions are a result of the imposed global C^1 -regularity. This is different from [10], where the collocation conditions are imposed, which then imply the C^1 -regularity. The different construction is due to the nonlinear character of the system. For simplicity regarding the prescription of inhomogeneous boundary conditions we make the following assumption.

Assumption 3.1: Inhomogeneous Dirichlet Boundary conditions

We impose an implicit restriction on the set of admissible boundary conditions g^e . We assume that there exists a function $g_{\tau,h}$ in $C^1(\bar{I}; \mathcal{V}_h)$ such that

$$g_{\tau,h}|_{\Gamma_D} = g^e \quad \forall t \in \bar{I}.$$

For prescribing more general boundary conditions suitable interpolation operators applied to the boundary values are required. For brevity and since this is a standard technique, it is not considered here.

We let $(\mathbf{e}_{0,h}, \mathbf{a}_{0,h}, \mathbf{p}_{0,h}, \mathbf{u}_{0,h}) =: \mathbf{v}_{0,h} \in (\mathcal{V}_h)^4$, which are appropriate finite element approximations of the initial values \mathbf{v}_0 . Here, we use interpolation in \mathcal{V}_h . We introduce

$$\partial_t^i \mathbf{w}_{n,h} = \partial_t^i \mathbf{w}_{\tau,h}(t_n), \quad (3.4)$$

and discretize Problem 2.2 with the GCC¹(3) method. From the local problems A.1 we derive the following global in time fully discrete formulation.

Problem 3.1: C^1 -regular in time Galerkin-collocation scheme for (2.4)

For given data and boundary conditions $\mathbf{f}_{\tau,h}, g_{\tau,h}^e \in C^1(\bar{I}; \mathcal{V}_{h,0})$, find $\mathbf{u}_{\tau,h}, \mathbf{p}_{\tau,h}, \mathbf{a}_{\tau,h}$ and $\mathbf{e}_{\tau,h}$ such that $\mathbf{e}_{\tau,h} = g_{\tau,h}^e$ on $\bar{I} \times \Gamma_D$ and for all $(\boldsymbol{\phi}_{1,h}^0, \dots, \boldsymbol{\phi}_{1,h}^{11}, \dots, \boldsymbol{\phi}_{N,h}^0, \dots, \boldsymbol{\phi}_{N,h}^{11}, \boldsymbol{\phi}_{\tau,h}^0, \dots, \boldsymbol{\phi}_{\tau,h}^3) =: \boldsymbol{\phi}_{\tau,h} \in \mathcal{V}_{h,0}^{12N} \times \mathbf{Y}_{\tau,h}^4$

$$\mathcal{A}_{\tau,h}(\mathbf{v}_{\tau,h})(\boldsymbol{\phi}_{\tau,h}) = \mathbf{F}_{\tau,h}(\boldsymbol{\phi}_{\tau,h}), \quad (3.5)$$

is satisfied, where $\mathbf{F} : \mathbf{Y}_{\tau,h}^4 \rightarrow \mathbb{R}$ and $\mathcal{A} : \mathbf{X}_{\tau,h}^4 \times (\mathcal{V}_h^{12N} \times \mathbf{Y}_{\tau,h}^4) \rightarrow \mathbb{R}$ are given by

$$\begin{aligned} \mathcal{A}_{\tau,h}(\mathbf{v}_{\tau,h})(\boldsymbol{\phi}_{\tau,h}) := & \int_0^T \langle \partial_t \mathbf{p}_{\tau,h}, \boldsymbol{\phi}_{\tau,h}^0 \rangle + \Gamma_0 \langle \mathbf{p}_{\tau,h}, \boldsymbol{\phi}_{\tau,h}^0 \rangle - \langle \mathbf{u}_{\tau,h}, \boldsymbol{\phi}_{\tau,h}^0 \rangle dt \\ & + \int_0^T v_t^2 \langle \mathbf{p}_{\tau,h}, \boldsymbol{\phi}_{\tau,h}^1 \rangle - \varepsilon_\Delta v_t^2 \langle \mathbf{e}_{\tau,h}, \boldsymbol{\phi}_{\tau,h}^1 \rangle + \langle \partial_t \mathbf{u}_{\tau,h}, \boldsymbol{\phi}_{\tau,h}^1 \rangle dt \\ & + \int_0^T \varepsilon_\omega \langle \partial_t \mathbf{e}_{\tau,h}, \boldsymbol{\phi}_{\tau,h}^2 \rangle - \Gamma_0 \langle \mathbf{p}_{\tau,h}, \boldsymbol{\phi}_{\tau,h}^2 \rangle + \chi^{(2)} \langle \partial_t (|\mathbf{e}_{\tau,h}| \mathbf{e}_{\tau,h}), \boldsymbol{\phi}_{\tau,h}^2 \rangle - \langle \mathbf{a}_{\tau,h}, \boldsymbol{\phi}_{\tau,h}^2 \rangle dt \\ & + \int_0^T \langle \nabla \mathbf{e}_{\tau,h}, \nabla \boldsymbol{\phi}_{\tau,h}^3 \rangle + \varepsilon_\Delta v_t^2 \langle \mathbf{e}_{\tau,h}, \boldsymbol{\phi}_{\tau,h}^3 \rangle - v_t^2 \langle \mathbf{p}_{\tau,h}, \boldsymbol{\phi}_{\tau,h}^3 \rangle + \langle \partial_t \mathbf{a}_{\tau,h}, \boldsymbol{\phi}_{\tau,h}^3 \rangle dt \end{aligned} \quad (3.6a)$$

$$\begin{aligned} & + \langle \mathbf{u}_{\tau,h}(0), \boldsymbol{\phi}_{\tau,h}^0(0) \rangle + \langle \mathbf{p}_{\tau,h}(0), \boldsymbol{\phi}_{\tau,h}^1(0) \rangle + \langle \mathbf{a}_{\tau,h}(0), \boldsymbol{\phi}_{\tau,h}^2(0) \rangle + \langle \mathbf{e}_{\tau,h}(0), \boldsymbol{\phi}_{\tau,h}^3(0) \rangle \\ & + \langle \partial_t \mathbf{u}_{\tau,h}(0), \boldsymbol{\phi}_{\tau,h}^4(0) \rangle + \langle \partial_t \mathbf{p}_{\tau,h}(0), \boldsymbol{\phi}_{\tau,h}^5(0) \rangle + \langle \partial_t \mathbf{a}_{\tau,h}(0), \boldsymbol{\phi}_{\tau,h}^6(0) \rangle + \langle \partial_t \mathbf{e}_{\tau,h}(0), \boldsymbol{\phi}_{\tau,h}^7(0) \rangle \end{aligned} \quad (3.6b)$$

$$\begin{aligned}
& + \sum_{n=1}^N \left(\langle \partial_t \mathbf{p}_{n,h}, \boldsymbol{\phi}_{n,h}^8 \rangle + \Gamma_0 \langle \mathbf{p}_{n,h}, \boldsymbol{\phi}_{n,h}^8 \rangle - \langle \mathbf{u}_{n,h}, \boldsymbol{\phi}_{n,h}^8 \rangle \right. \\
& + v_t^2 \langle \mathbf{p}_{n,h}, \boldsymbol{\phi}_{n,h}^9 \rangle - \varepsilon_\Delta v_t^2 \langle \mathbf{e}_{n,h}, \boldsymbol{\phi}_{n,h}^9 \rangle + \langle \partial_t \mathbf{u}_{n,h}, \boldsymbol{\phi}_{n,h}^9 \rangle \\
& + \varepsilon_\omega \langle \partial_t \mathbf{e}_{n,h}, \boldsymbol{\phi}_{n,h}^{10} \rangle - \Gamma_0 \langle \mathbf{p}_{n,h}, \boldsymbol{\phi}_{n,h}^{10} \rangle + \chi^{(2)} \langle \partial_t (\mathbf{e}_{n,h} | \mathbf{e}_{n,h}), \boldsymbol{\phi}_{n,h}^{10} \rangle - \langle \mathbf{a}_{n,h}, \boldsymbol{\phi}_{n,h}^{10} \rangle \\
& \left. + \langle \nabla \mathbf{e}_{n,h}, \nabla \boldsymbol{\phi}_{n,h}^{11} \rangle + \varepsilon_\Delta v_t^2 \langle \mathbf{e}_{n,h}, \boldsymbol{\phi}_{n,h}^{11} \rangle - v_t^2 \langle \mathbf{p}_{n,h}, \boldsymbol{\phi}_{n,h}^{11} \rangle + \langle \partial_t \mathbf{a}_{n,h}, \boldsymbol{\phi}_{n,h}^{11} \rangle \right), \quad (3.6c)
\end{aligned}$$

$$\mathbf{F}_{\tau,h}(\boldsymbol{\phi}_{\tau,h}) := \int_0^T \langle \mathbf{f}_{\tau,h}, \boldsymbol{\phi}_{\tau,h}^3 \rangle dt + \sum_{n=1}^N \langle \mathbf{f}_{\tau,h}(t_n), \boldsymbol{\phi}_{n,h}^3 \rangle \quad (3.6d)$$

$$\begin{aligned}
& + \langle \mathbf{u}_{0,h}, \boldsymbol{\phi}_{\tau,h}^0(0) \rangle + \langle \mathbf{p}_{0,h}, \boldsymbol{\phi}_{\tau,h}^1(0) \rangle + \langle \mathbf{a}_{0,h}, \boldsymbol{\phi}_{\tau,h}^2(0) \rangle + \langle \mathbf{e}_{0,h}, \boldsymbol{\phi}_{\tau,h}^3(0) \rangle \\
& + \langle \partial_t \mathbf{u}_{0,h}, \boldsymbol{\phi}_{\tau,h}^4(0) \rangle + \langle \partial_t \mathbf{p}_{0,h}, \boldsymbol{\phi}_{\tau,h}^5(0) \rangle + \langle \partial_t \mathbf{a}_{0,h}, \boldsymbol{\phi}_{\tau,h}^6(0) \rangle + \langle \partial_t \mathbf{e}_{0,h}, \boldsymbol{\phi}_{\tau,h}^7(0) \rangle. \quad (3.6e)
\end{aligned}$$

In our implementation, we use a local test basis supported on the subintervals I_n in Problem 3.1. This leads to a time marching scheme with the local Problem A.1 to be solved in each of the time steps. We comment on the fully discrete Problem 3.1.

- In contrast to [4], collocation conditions are a result of the imposed global C^1 -regularity. As already mentioned in [4, Remark 3.4] the approach of imposing global C^1 -regularity is also valid. We also show this in detail in Appendix A.
- After breaking Problem 3.1 into local problems, we can put the equations of the proposed GCC¹(3) approach in their algebraic forms (cf. Appendix A) and get a nonlinear system of equations. The common approach of handling the nonlinear problem is a linearization by means of Newton's method. In every Newton step we have to solve a linear system of equations, of which we give a detailed description in the Appendix A.
- Hermite polynomials are ideal for wave problems, particularly those with high frequencies. Moreover, they offer significant advantages for the numerical solution of the nonlinear wave equations (2.2) by reducing the computational cost of assembling matrices and residuals in Newton's method. These advantages result from the sparse structure of the nonlinear term given by Hermite polynomials as trial functions:

$$\begin{aligned}
\int_{I_n} \chi^{(2)} \langle \partial_t (|\mathbf{e}| \mathbf{e}), \zeta_1 \rangle dt &= \chi^{(2)} (|\mathbf{e}_0| |\mathbf{e}_1| |\mathbf{e}_2| |\mathbf{e}_3|)^\top \underbrace{\int_{I_n} (\partial_t (\xi_i \xi_j))_{i,j=0,\dots,3} dt}_{=\text{diag}((-1, 0, 1, 0)) \in \mathbb{R}^{4 \times 4}} (\mathbf{e}_0 \ \mathbf{e}_1 \ \mathbf{e}_2 \ \mathbf{e}_3) \\
&= \chi^{(2)} |\mathbf{e}_2| \mathbf{e}_2 - \chi^{(2)} |\mathbf{e}_0| \mathbf{e}_0,
\end{aligned}$$

where $\{\mathbf{e}_i\}_{i=0}^3$ denote the coefficient functions of the i -th time basis function in \mathcal{V}_h . This also applies to third order nonlinearities $\chi^{(3)}$ with two non-vanishing terms.

$$\begin{aligned}
\int_{I_n} \chi^{(3)} \langle \partial_t (|\mathbf{e}|^2 \mathbf{e}), \zeta_1 \rangle dt &= \chi^{(3)} (|\mathbf{e}_0|^2 |\mathbf{e}_1|^2 |\mathbf{e}_2|^2 |\mathbf{e}_3|^2)^\top \int_{I_n} (\partial_t (\xi_i \xi_j \xi_k))_{i,j,k=0,\dots,3} (\mathbf{e}_0 \ \mathbf{e}_1 \ \mathbf{e}_2 \ \mathbf{e}_3) \\
&= \chi^{(3)} |\mathbf{e}_2|^2 \mathbf{e}_2 - \chi^{(3)} |\mathbf{e}_0|^2 \mathbf{e}_0.
\end{aligned}$$

We consider the abstract space-time discrete form (3.5). The global formulation puts the work in this section in context to the abstract problem introduced in Definition 2.2 and, together with an analogous formulation of the solution operator, becomes useful in the next section.

Definition 3.1: Discrete Solution Operator

Consider Problem 3.1 given in variational formulation. Then the solution operator $\mathcal{S}_{\tau,h}$ to (3.5), which maps $g_{\tau,h}^e$, $\mathbf{f}_{\tau,h}$ and the initial conditions $\mathbf{v}_{0,h}$ to the solution $\mathbf{v}_{\tau,h}$ is defined through

$$\begin{aligned} \mathcal{S}_{\tau,h} : D(\mathcal{S}_{\tau,h}) \subset C^1(\bar{I}; \mathcal{V}_h) \times C^1(\bar{I}; \mathcal{V}_{h,0}) \times \mathcal{V}_h^4 &\rightarrow \mathbf{X}_{\tau,h}^4, \\ (g_{\tau,h}^e, \mathbf{f}_{\tau,h}, \mathbf{v}_{0,h}) &\mapsto \mathbf{v}. \end{aligned} \quad (3.7)$$

In order to ensure well-posedness we assume that $\mathcal{S}_{\tau,h}$ is a bijection. Then, for given data $\mathbf{f}_{\tau,h}$ we find a unique solution $(\mathbf{e}_{\tau,h}, \mathbf{a}_{\tau,h}, \mathbf{p}_{\tau,h}, \mathbf{u}_{\tau,h}) = \mathbf{v}_{\tau,h} \in \mathbf{X}_{\tau,h}^4$ which satisfies $\mathcal{S}_{\tau,h}(g_{\tau,h}^e, \mathbf{f}_{\tau,h}, \mathbf{v}_{0,h}) = \mathbf{v}_{\tau,h}$. We note that $\mathcal{S}_{\tau,h}$, $\mathbf{v}_{\tau,h}$, $g_{\tau,h}^e$ and $\mathbf{f}_{\tau,h}$ approximate \mathcal{S} , \mathbf{v} and \mathbf{f} in (2.6). In the next section we introduce two types of ANNs, which we consider for training a discrete solution operator

$$\mathcal{U} \approx \mathcal{S}_{\tau,h}. \quad (3.8)$$

\mathcal{U} is trained with accurate approximations $\mathbf{v}_{\tau,h}$ obtained by numerical solutions and is subsequently used to solve an optimal control problem.

4. Artificial Neural Networks

Neural networks exist in various types. In this section we briefly review the architecture of the neural networks that we use below to learn the discrete solution operator defined in Problem 3.1. In Section 5, the neural networks are then applied to accelerate optimization processes for Dirichlet boundary control of the pump pulse for terahertz generation.

4.1. Fourier Neural Operators (FNO)

FNO is a recently introduced type of ANN that proposes a novel method for combining neural networks with Fourier analysis, mainly to solve differential equations [57]. Within the framework of Neural Operators, a universal approximation theorem and error bounds have been developed for the FNO in [52]. The key innovation of the FNO is a new type of layer, the Fourier layer (cf. Fig. 2 and (4.6)). In the Fourier layer the Fourier series is used to efficiently compute the convolution of the input function with a set of integration kernels, represented in the frequency domain.

Here, we briefly introduce FNOs for complex-valued functions $\mathbf{v} \in L^1(\mathbb{T}^d)$ on the unit torus \mathbb{T}^d , in order to restrict ourselves to 1-periodic functions. For details we refer to [36, Section 3.1]. The Fourier transform of a function $\mathbf{v} : \mathbb{T}^d \rightarrow \mathbb{C}^n$ is denoted by $\mathcal{F} : L^2(\mathbb{T}^d; \mathbb{C}^n) \rightarrow \ell^2(\mathbb{Z}^d; \mathbb{C}^n)$. Similarly, $\mathcal{F}^{-1} : \ell^2(\mathbb{Z}^d; \mathbb{C}^n) \rightarrow L^2(\mathbb{T}^d; \mathbb{C}^n)$ denotes the Fourier inversion. More precisely, for a function $v \in L^2(\mathbb{T}^d; \mathbb{C})$ the Fourier transform is defined by (cf. [36, Definition 3.1.1])

$$(\mathcal{F}v)(l) = \int_{\mathbb{T}^d} v(x) \exp(-2\pi i \langle l, x \rangle) dx, \quad l \in \mathbb{Z}^d. \quad (4.1)$$

For a function $w \in \ell^2(\mathbb{Z}^d; \mathbb{C})$ is given by Fourier inversion (cf. [36, Proposition 3.2.5]) by

$$(\mathcal{F}^{-1}w)(x) = \sum_{l \in \mathbb{Z}^d} w(l) \exp(2\pi i \langle l, x \rangle), \quad x \in \mathbb{T}^d. \quad (4.2)$$

For vector-valued functions, the formulas (4.1) and (4.2) are applied componentwise. We note that, for an integrable function \mathbf{u} on \mathbb{R}^n with Fourier transform $\hat{\mathbf{u}}$, the Fourier series and Fourier inversion

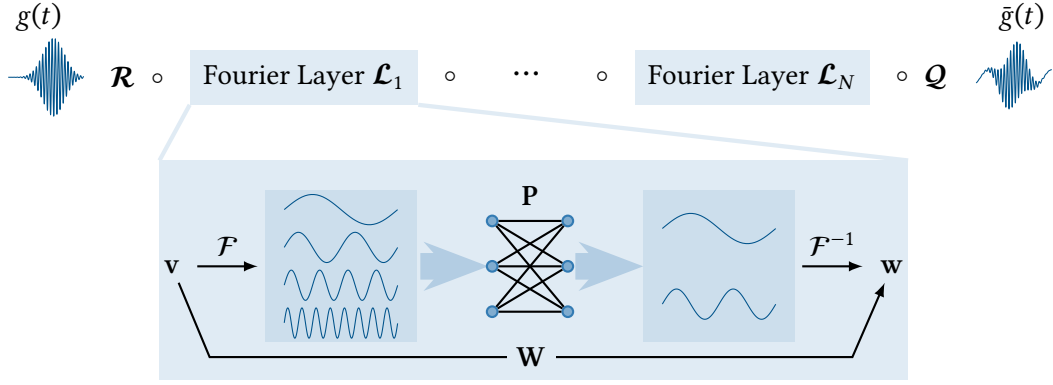


Figure 2: Sketch of the FNO. First, the input is lifted to a higher dimensional space by \mathbf{R} , which is defined in (4.4). Then apply the Fourier layers (4.6) and finally project onto the target by \mathbf{Q} , as defined in (4.5). In the Fourier layer defined by (4.6), a Fourier Transform \mathcal{F} is applied and a linear transform filters out the higher modes. Then, the inverse Fourier transform \mathcal{F}^{-1} is applied. A linear transform \mathbf{W} acts similar to a skip connection.

can be seen as the restriction of the classical Fourier transform to \mathbb{Z}^n . Together with the Poisson summation formula [36, Theorem 3.2.8], we know that the Fourier expansion equals the periodization of the function v on \mathbb{R}^n . This gives us a perspective on the extension of the Fourier series, and therefore FNOs, to non-periodic functions.

Definition 4.1: Fourier Neural Operator (FNO)

An FNO $\mathcal{N} : L^2(\mathbb{T}^d, \mathbb{R}^{d_i}) \rightarrow L^2(\mathbb{T}^d, \mathbb{R}^{d_o})$ is a mapping consisting of a concatenation of functions such that

$$\mathcal{N}(\mathbf{v}) = \mathbf{Q} \circ \mathcal{L}_N \circ \dots \circ \mathcal{L}_1 \circ \mathbf{R}(\mathbf{v}), \quad (4.3)$$

with a lifting operator \mathbf{R} and a projection operator \mathbf{Q} , represented by matrices $\mathbf{R} \in \mathbb{R}^{n \times d_i}$ and $\mathbf{Q} \in \mathbb{R}^{d_o \times n}$, respectively

$$\begin{aligned} \mathbf{R} : L^2(\mathbb{T}^d; \mathbb{R}^{d_i}) &\rightarrow L^2(\mathbb{T}^d; \mathbb{R}^n), & \mathbf{Q} : L^2(\mathbb{T}^d; \mathbb{R}^n) &\rightarrow L^2(\mathbb{T}^d; \mathbb{R}^{d_o}), \\ \mathbf{v} &\mapsto \mathbf{R}\mathbf{v}, & \mathbf{v} &\mapsto \mathbf{Q}\mathbf{v}, \end{aligned} \quad (4.4) \quad (4.5)$$

$$(\mathbf{R}v)(x) = \mathbf{R}(v(x)), \quad \mathbf{R} \in \mathbb{R}^{n \times d_i}. \quad (\mathbf{Q}v)(x) = \mathbf{Q}(v(x)), \quad \mathbf{Q} \in \mathbb{R}^{d_o \times n}.$$

A Fourier layer \mathcal{L}_k is given by

$$\mathcal{L}_k(\mathbf{v}) = \sigma \left(\mathbf{W}_k \mathbf{v} + \mathbf{b}_k + \underbrace{\mathcal{F}^{-1} (P_n \mathcal{F}(\mathbf{v}))}_{\mathcal{K}_n \mathbf{v}} \right), \quad (4.6)$$

where $\mathbf{W}_k \in \mathbb{R}^{n \times n}$ is a weight matrix and $\mathbf{b}_k \in \mathbb{R}^n$ a bias vector and $P_n : \mathbb{Z}^d \rightarrow \mathbb{C}^{n \times n}, l \mapsto P_n(l) \in \mathbb{C}^{n \times n}$ are the weights of the modes $l \in \mathbb{Z}^d$ and $\sigma : \mathbb{R}^n \rightarrow \mathbb{R}^n$ is an activation function, for instance the tanh function is applied.

Concerning Definition 4.1 we note the following.

- Let us consider $(\mathcal{F}\mathbf{v})(l) \in \mathbb{C}^n$. In order to ensure that $\mathcal{K}_n \mathbf{v}$ in (4.6) is real-valued for real-valued \mathbf{v}

conjugate symmetry in the parametrization is enforced by

$$P_n(-l)_{j,k} = P_n^*(l)_{j,k}, \quad j = 1, \dots, m, \quad k = 1, \dots, n \quad \forall l \in Z_{l_{\max}}; \quad (4.7)$$

- In (4.4) and (4.5), \mathcal{R} and \mathcal{Q} are both locally acting operators. They are represented by the matrices \mathbf{R} and \mathbf{Q} , that are to be trained.
- We restrict the domain of the FNO to \mathbb{T}^d , in order to consider only 1-periodic functions. The Poisson summation formula lets us lift this restriction. Similarly, in [52, Lemma 41] the authors show that FNOs can be generalized to domains with Lipschitz boundary.
- The activation function $\sigma : \mathbb{R}^n \rightarrow \mathbb{R}^n$ with $\sigma \mathbf{v} = (\sigma(v_1), \dots, \sigma(v_n))^T \in \mathbb{R}^n$ is a componentwise applied scalar- and real-valued, non-polynomial function $\sigma \in C^\infty(\mathbb{R})$, which is globally Lipschitz-continuous.

We sketch the FNO in Fig. 2. The key feature of FNO architectures are the convolution-based integral kernels \mathcal{K}_n , that are non-local. This enables learning operators with a global character, such as operators arising in the simulation of PDEs. Another major factor in the efficiency is that in the discrete case we are able to use the Fast Fourier Transform (FFT) to compute $\mathcal{K}_n \mathbf{v}$ in (4.6), if the computational mesh is uniform. This is sketched in the following.

The Discrete Setting

Let the $D_J \subset \mathbb{T}^d$ be a set of $J \in \mathbb{N}$ uniformly distributed points with resolution $s_1 \times \dots \times s_d = J$ in the domain \mathbb{T}^d , $v \in \mathbb{C}^{J \times n}$ and $\mathcal{F}(v) \in \mathbb{C}^{J \times n}$. The multiplication by the weight tensor $P \in \mathbb{C}^{J \times m \times n}$ is defined by the operation

$$(P \cdot (\mathcal{F}v))_{k,l} = \sum_{j=1}^n P_{k,l,j} (\mathcal{F}v)_{k,j}, \quad k = 1, \dots, J, \quad l = 1, \dots, m. \quad (4.8)$$

The Fourier transform \mathcal{F} can be replaced by the Fast Fourier Transform (FFT). For $v \in \mathbb{C}^{J \times n}$, $k = (k_1, \dots, k_d) \in \mathbb{Z}_{s_1} \times \dots \times \mathbb{Z}_{s_d}$, and $x = (x_1, \dots, x_d) \in \mathbb{T}^d$, the FFT $\widehat{\mathcal{F}}$ and its inverse $\widehat{\mathcal{F}}^{-1}$ are defined as

$$\begin{aligned} (\widehat{\mathcal{F}}v)_l(k) &= \sum_{x_1=0}^{s_1-1} \dots \sum_{x_d=0}^{s_d-1} v_l(x_1, \dots, x_d) \exp\left(-2i\pi \sum_{j=1}^d \frac{x_j k_j}{s_j}\right), \quad \text{for } l = 1, \dots, n, \\ (\widehat{\mathcal{F}}^{-1}v)_l(x) &= \sum_{k_1=0}^{s_1-1} \dots \sum_{k_d=0}^{s_d-1} v_l(k_1, \dots, k_d) \exp\left(2i\pi \sum_{j=1}^d \frac{x_j k_j}{s_j}\right), \quad \text{for } l = 1, \dots, n. \end{aligned}$$

The parameters \mathbf{W} , \mathbf{b} , \mathbf{P} of the Fourier layers in Definition 4.1 are learned in Fourier space, where they can be expressed in terms of the Fourier coefficients of the input functions. When the network is used to evaluate functions in physical space, it simply amounts to projecting onto the basis functions $\exp(2\pi i \langle x, k \rangle)$, which are well-defined for all $x \in \mathbb{C}^d$. This allows the network to evaluate functions at any desired resolution, without being tied to a specific discretization scheme. The implementation of the FNO using the FFT restricts the geometry and discretization to uniform mesh discretizations of \mathbb{T}^d . In practice FNOs can be extended to other domains by padding the input with zeros. The loss is computed only on the original domain during training. The Fourier neural operator extends the output smoothly to the padded domain, as discussed in [53].

4.2. Recurrent neural networks with memory

Recurrent neural networks (RNNs) are an extension to Feed-forward neural networks that use an activation variable $\mathbf{a}_n^k \in \mathbb{R}^{p_k}$ to propagate information over discrete time steps, making them suitable for time series and sequential data. An extension of this model uses network nodes with memory. These neural networks are effective in modeling long-term dependencies and can overcome the vanishing gradient problem that recursive neural networks face [42]. In our work, we employ Gated Recurrent Units (GRUs) [21].

Definition 4.2: Gated Recurrent Unit (GRU)

A Gated Recurrent Neural Network $\mathcal{N} : X^N \rightarrow Y^N$ maps a sequence of elements of a finite dimensional inner product space X to a sequence of elements of a finite dimensional inner product space Y . It consists of a concatenation multiple GRUs, i.e.

$$\mathcal{N} = \mathcal{G}_1 \circ \dots \circ \mathcal{G}_L \quad (4.9)$$

A GRU $\mathcal{G}_k : \mathbb{R}^N \times \mathbb{R}^q \rightarrow \mathbb{R}^{N \times q} \times \mathbb{R}^q$, $k \in \{1, \dots, L\}$ is defined by the following equations:

$$\mathbf{z}_n^k = \sigma_z(\mathbf{W}_k^{(z)} \mathbf{h}_n^{k-1} + \mathbf{U}_k^{(z)} \mathbf{h}_{n-1}^k + \mathbf{b}_k^{(z)}), \quad (4.10a)$$

$$\mathbf{r}_n^k = \sigma_r(\mathbf{W}_k^{(r)} \mathbf{h}_n^{k-1} + \mathbf{U}_k^{(r)} \mathbf{h}_{n-1}^k + \mathbf{b}_k^{(r)}), \quad (4.10b)$$

$$\mathbf{h}_n^k = \mathbf{z}_n^k \odot \mathbf{h}_{n-1}^k + (1 - \mathbf{z}_n^k) \odot \sigma_h(\mathbf{W}_k^{(h)} \mathbf{h}_n^{k-1} + \mathbf{U}_k^{(h)}(\mathbf{r}_n^k \odot \mathbf{h}_{n-1}^k) + \mathbf{b}_k^{(h)}), \quad (4.10c)$$

where $n \in \{1, \dots, N\}$, \odot denotes the element-wise product and $\mathbf{U}_k^{(\cdot)}$, $\mathbf{W}_k^{(\cdot)}$ and $\mathbf{b}_k^{(\cdot)}$ are weight matrices and bias vectors determined by training. By \mathbf{h}_n^0 we denote the input to the GRU.

In (4.10), the update gate vector $\mathbf{z}_n^k \in \mathbb{R}^q$ defined in (4.10a) determines the contribution of the previous hidden output \mathbf{h}_{n-1}^k to the current output \mathbf{h}_n^k (cf. (4.10a)), while the reset gate vector $\mathbf{r}_n^k \in \mathbb{R}^q$ defined by (cf. (4.10b)) controls the nonlinearity of the cell. Together, they control the memory of a GRU cell, determining to what extent information from the past is carried over to the present output.

5. Optimal control with Neural Operators

Optimal control problems (OCP) are important in several branches of science and engineering. Finding efficient solutions to these problems remains a challenging task. Neural operators can represent the dynamics of complex systems efficiently. Their combination with OCPs has the potential to yield novel solutions by replacing the oftentimes costly solution of the forward problem. In this section, we investigate the use of neural operators for solving OCPs, with a focus on Dirichlet boundary conditions as constraints. We apply this technique to the problem of THz generation in a periodically poled crystal (cf. Section 2.1) and propose a novel approach to optimize the input pulse with the goal to maximize the efficiency of optical to THz generation. This can be formulated as an optimal boundary control problem, where we seek the Dirichlet boundary conditions that yield the maximum optical to THz conversion.

5.1. Optimal Dirichlet boundary control

First, we state a general optimal Dirichlet boundary control problem, which serves as the foundation for our proposed method.

Definition 5.1: Function spaces for optimal control problem

Define $S = I \times \Gamma_D$ and $Q = I \times \mathcal{D}$ and the set of admissible controls

$$U_{\text{ad}} = \left\{ u \in L^2(S) \mid u_a \leq u \leq u_b \text{ a. e. in } S, u_a, u_b \in L^2(S) \right\}. \quad (5.1)$$

Let \mathcal{J} be a Gateaux differentiable functional. For the state $\mathbf{y} \in W(I)$ and the control $u \in U_{\text{ad}}$ we consider the following optimization problem.

Problem 5.1: Optimal Dirichlet boundary control

For $\mathcal{J} : \mathbf{W}(I) \times L^2(S) \rightarrow \mathbb{R}$, $(\mathbf{y}, u) \mapsto \mathcal{J}(\mathbf{y}, u)$ solve

$$\min_{u \in U_{\text{ad}}} \mathcal{J}(\mathbf{y}, u) = \mathcal{G}(\mathbf{y}) + \frac{\alpha}{2} \|u\|^2, \quad \alpha > 0, \quad (5.2a)$$

$$\text{subject to} \quad \mathbf{y} = \mathbf{S}(u, \mathbf{f}, \mathbf{y}_0). \quad (5.2b)$$

The operator \mathbf{S} is the abstract solution operator of the PDE introduced for our application in (2.6), by which the optimization problem is constrained. The control u enters through the Dirichlet boundary condition. The functional $\mathcal{G} : \mathbf{W}(I) \rightarrow \mathbb{R}$ is left to be defined for the application.

We now derive an OCP similar to Problem 5.1 for a setting where Problem 2.1 provides the initial and boundary conditions and the PDE for the optimization problem. In practice, we define the functional \mathcal{G} in (5.2a) such that radiation at frequency f_Ω is optimized. Since $\max \mathcal{J} = -\min(-\mathcal{J})$ is satisfied, we restrict ourselves to the description of minimization problems.

Definition 5.2: Cost function for optimizing generation of THz radiation

Let $y_c : W_{\text{nl}}(I) \rightarrow L^2(I; \mathbb{R})$ and $\psi : \mathbb{R} \rightarrow \mathbb{R}$ be given by

$$y_c(\mathbf{y}) = \int_{B_\epsilon(c)} \mathbf{y}(x, t) \, dx, \quad (5.3)$$

$$\psi(v) = \mathbf{1}_{(f_\Omega-r, f_\Omega+r)} \exp\left(\frac{r^2}{(v-r-f_\Omega)(v+r+f_\Omega)}\right), \quad r > 0, \quad (5.4)$$

where the ball $B_\epsilon(c)$ around the control point $c \in \mathcal{D}$ is chosen such that $B_\epsilon(c) \cap \Gamma_D = \emptyset$ is satisfied. We define the cost functional \mathcal{G} as

$$\mathcal{G}_\Omega(\mathbf{y}) = \int_{f_\Omega-r}^{f_\Omega+r} \mathcal{F}(y_c(\mathbf{y}, t))(v)^2 \psi(v) \, dv. \quad (5.5)$$

We note that $y_c \in L^2(I; \mathbb{R})$ and therefore its Fourier transform exists. The parameter r is chosen such that ψ is sufficiently close to the indicator function at f_Ω . In the discrete case, we specify this more precisely. For the state $\mathbf{e} \in W_{\text{nl}}(I)$ and the control $g^\mathbf{e} \in U_{\text{ad}}$ we study the following optimization problem.

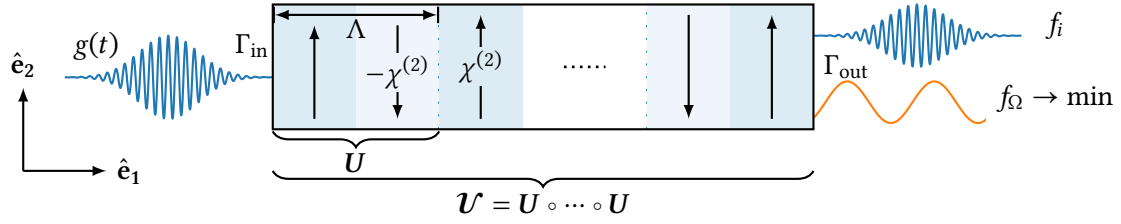


Figure 3: Sketch of using ANNs for the simulation of wave propagation in periodically poled nonlinear materials. The solution operator U , solves the wave equation (2.2a) over one period. U is learned from simulation data generated by space-time FEM. The training data for the U is collected at the interfaces of two periods, which are separated by a distance of Λ .

Problem 5.2: Optimal Dirichlet boundary control for THz generation

For the solution operator (2.6) to Problem 2.2, solve the optimization problem

$$\begin{aligned} \max_{u \in U_{\text{ad}}} \quad & \mathcal{J}(\mathbf{e}, g^e) = \mathcal{G}_{\Omega}(\mathbf{e}) + \frac{\alpha}{2} \|g^e\|^2, \quad (5.6a) \\ \text{subject to} \quad & (\mathbf{u}, \mathbf{p}, \mathbf{a}, \mathbf{e})^{\top} = \mathcal{S}(g^e, \mathbf{f}, \mathbf{v}_0). \end{aligned}$$

We provide realistic parameters for this problem in Section 6. In the formulation of Problem 5.2, we can replace the solution operator \mathcal{S} , the data \mathbf{f} , and \mathbf{v}_0 with their discrete counterparts as defined in Definition 3.1 in a straightforward manner. We can evaluate the cost function in the discrete setting using an FFT. While different methods exist for the solution of OCPs similar to 5.1, to the best of our knowledge the nonlinear wave equation of Problem 5.2 has not yet been investigated in theory or practice. Within this work we concentrate on the algorithmic and practical aspects of solving Problem 5.1. For an overview over optimal control theory and solution methods we refer to [41, 64] and references therein and, more specifically for hyperbolic problems, to [38].

5.2. Optimal Control for THz generation with Neural operators

Even in one space dimension solving Problem 5.2 by using the variational space-time methods we presented so far is infeasible for scenarios of practical interest due to the substantial computational burden imposed by the solution of the forward problem; cf. [65]. In order to focus the presentation on the essential ideas, we restrict ourselves to the one-dimensional case for the remainder of this section. In [65] we observed that this is a reasonable restriction to make from a practical point of view.

We propose an algorithm that relies on ANNs to accelerate the solution of the PDE, allowing for a more efficient optimization of the control parameters. In Fig. 3 we sketch its key idea. The goal is to train neural operators \mathcal{U} based on accurate numerical simulations which generalize well to U_{ad} . Then they are used as the forward solver in the optimal Dirichlet boundary control problem. The first cornerstone of the method is to consider only controls that are feasible in practice. By this we can implement a differentiable sampler of Dirichlet boundary data in a deep learning library of our choice and concatenate it with the solution operator.

Definition 5.3: Admissible controls for Problem 5.2

The Dirichlet data, i. e. the control in Problem 5.2, is of the form

$$g(t) = \exp\left(-\left(2 \log 2 \left(\frac{t}{\tau}\right)^2\right)^p\right) \sum_{i=1}^n a_i \cos\left(\varphi_i + 2\pi \left(\frac{1}{2}\zeta_i t^2 + f_i t\right)\right). \quad (5.7a)$$

For some fixed n the set of parameters Ξ and a sampler \mathcal{P} which maps these parameters to the pulses are given by

$$\Xi = \left\{ (\tau, p, a_0, \varphi_0, \zeta_0, f_0, \dots, a_n, \varphi_n, \zeta_n, f_n) \in \mathbb{R}_+^{2+4n} \mid \tau \leq \tau_{\max}, p \leq p_{\max}, \right. \\ \left. a_i \leq a_{\max}, \varphi_i \leq \varphi_{\max}, \zeta_i \leq \zeta_{\max}, f_i \leq f_{\max} \forall i = 1, \dots, n \right\}, \quad (5.7b)$$

$$\mathcal{P} : \Xi \rightarrow L^2(\Gamma_{\text{in}} \times I), (\tau, p, a_0, \varphi_0, \zeta_0, f_0, \dots, a_n, \varphi_n, \zeta_n, f_n) \mapsto g(t). \quad (5.7c)$$

In (5.7), the parameter τ is the full width half maximum, p the order of the supergaussian, a_i the amplitude, φ_i the phaseshift, ζ_i the quadratic chirprate and f_i the center frequency. The upper bounds in (5.7b) are given through the limitations of the experimental setup. Note that the image of $\mathcal{P}[\Xi] \subset L^2(S)$ is the set of admissible controls U_{ad} in Problem 5.2.

The second idea of the method is the differentiability of a program written with an established ANN library: For most operations on the datastructures of these libraries a method for calculating its gradient is already implemented. The last idea in our algorithm builds on the periodicity of the material parameters (cf. Fig. 3). The example in this work is based on periodically poled crystals, where $\chi^{(2)}$ govern the nonlinear processes. The periodicity of $\chi^{(2)}$ can be used to learn a solution operator U to the forward problem in only one period of the $\chi^{(2)}$ parameter. We formalize this concept in the discrete setting: Consider the discrete solution operator given in (3.7). The goal is to approximate $\mathcal{S}_{\tau, h}(g(t))$ by

$$U \circ \dots \circ U(g(t)) =: \mathcal{U} \approx \mathcal{S}_{\tau, h}(g(t)). \quad (5.8)$$

On the other hand, for the efficient solution of Problem 5.2 we don't need the full space-time solution. We only need the solution at some collocation points

$$J_{\mathcal{D}} = \bigcup_{i=1}^m \{x_{\mathcal{D}, i}\}, \quad x_{\mathcal{D}, i} := \Lambda i \in \mathcal{D}, \quad (5.9)$$

where m is the number of periods in the crystal. For the generation of training data we evaluate and save the solution $\mathbf{e}(x, t)$ at the points in $J_{\mathcal{D}}$. Motivated by the fact that $J_{\mathcal{D}, i+1}$ is the set $J_{\mathcal{D}, i}$, shifted in positive x_1 -direction, we construct an operator U which maps the time trajectory of the electric field \mathbf{e} at period i to the time trajectory of \mathbf{e} at period $i+1$. In order to construct a suitable solution operator we define the space

$$V_{\tau}(I) = \left\{ \mathbf{w} \in L^2(I; \mathbb{R}) \mid \mathbf{w}(t)|_{I_n} \in \mathbb{P}_3(I_n, \mathbb{R}) \right\}. \quad (5.10)$$

Definition 5.4: Neural Operator for Problem 5.2

Let $i \in \{1, \dots, m\}$, $x_a \in J_{\mathcal{D}, i}$, $x_b = x_a + \mathbf{e}_1 \Lambda \in J_{\mathcal{D}, i+1}$ and $p(t; x_a) \in V_{\tau}(I)$. The neural operator $U = \mathbf{I} \circ \mathcal{N} \circ \mathbf{T}$ is constructed such that

$$U : V_{\tau}(I) \rightarrow V_{\tau}(I), \\ \mathbf{p}(t; x_a) \mapsto \hat{\mathbf{p}}(t; x_b), \quad (5.11)$$

where \mathcal{N} is one of the networks introduced in Section 4, \mathbf{T} evaluates $\mathbf{p} \in V_\tau(I)$ at the endpoints of the subinterval and \mathbf{I} is the Hermite-type interpolator (A.8) applied on each subinterval I_n ,

$$\begin{aligned} \mathbf{T} : V_\tau &\rightarrow \mathbb{R}^{N+1}, \\ \mathbf{p}(t; x_a) &\mapsto (\mathbf{p}(t_0; x_a), \dots, \mathbf{p}(t_N; x_a)), \end{aligned} \quad (5.12)$$

$$\begin{aligned} \mathbf{I} : \mathbb{R}^{N+1} &\rightarrow V_\tau, \\ \mathbf{u} &\mapsto \hat{\mathbf{p}}(t; x_b). \end{aligned} \quad (5.13)$$

For the evaluation of \mathbf{I} we use automatic differentiation in order to obtain $\partial_t \mathcal{N}$. Further, we note that the coefficients of the polynomials and the values of $\hat{\mathbf{p}}$ at the time endpoints of I_n coincide, which makes the evaluation computationally cheap. With these preparations, the computation of $\mathbf{p}(t; x_a) = \mathbf{U}(g(t))$, $x_a \in J_{D,0} = \Gamma_{\text{in}}$ is well-defined and $\mathbf{p}(t; x_a + \Lambda)$ is the time trajectory of the electric field \mathbf{e} at period 1. We can iterate this to obtain the time trajectory at period i ,

$$\mathbf{p}_{i-1}(t; x_a + \Lambda(i-1)) = \mathbf{U}^{i-1}(g(t)) = \mathbf{p}_i(t; x_a + \Lambda i). \quad (5.14)$$

With the solution operator defined, we can formulate the algorithm for the solution of the optimal Dirichlet boundary control problem. Through the differentiability of $\mathcal{P} \circ \mathcal{U}$ we can calculate the gradients of the parameters $\xi \in \Xi$ with respect to the cost function in Problem 5.2. Then we can use the well-known gradient descent algorithm or Newton's method for the solution of Problem 5.2. In Algorithm 5.1 we describe the steps using a simple gradient descent method, which can also be tracked in Fig. 1. The extension to Newton's method is straightforward. In Appendix B we give an abstract formulation of how a solution operator for a full space-time approximation \mathcal{U} can be obtained.

Algorithm 5.1: Optimal control based on deep learning

```

1 function optimize-pulse-parameters( $\mathcal{P}, \mathcal{U}$ ) :  $\xi_{\text{opt}}$ 
2   Initialize pulse parameters  $\xi_0 \in \Xi$ , Set  $n = 0$ ;
3   do
4      $g(t) = \mathcal{P}(\xi)$ ; // Sample pulse
5      $\mathbf{e}(x, t) = \mathcal{U}(g)$ ; // Evaluate solution operator
6      $\delta\xi = \alpha \frac{\partial}{\partial \xi_n} \mathcal{G}_\Omega(\mathbf{e}(x, t))$ ; // Calculate update for gradient descent
7      $\xi_{n+1} = \xi_n + \delta\xi$ ; // Update pulse parameters
8      $n = n + 1$ ;
9   while  $|\delta\xi| > \varepsilon$ ;
10  Return  $\xi_{\text{opt}} = \xi_n$ ;
11 end

```

6. Numerical Experiments

We present numerical studies of the proposed neural operators for solving optimal control problems. First, we investigate and validate their ability to efficiently represent the dynamics of a simple test case. Then we extend the test to our method of optimal control via neural operators by adding a set of constraints and solving the resulting optimal control problem. Finally, we demonstrate the feasibility of the proposed approach by applying our methods to the physical problem of THz generation and compare the results to experimental data. In this section we only consider settings in one space dimension, since otherwise numerical simulations are too time-consuming. In [65] we also restricted ourselves to 1D without notable limitations.

6.1. Implementation aspects

We implemented our numerical simulations using deal . II [6], a finite element toolbox that offers efficient and scalable parallelization with MPI. To solve the nonlinear systems of equations, we employ a Newton-Krylov method. For the linear systems of equations that arise for each Newton iteration, we use the generalized minimal residual method (GMRES) with the algebraic multigrid solver MueLu [13]. MueLu serves as a preconditioner with a single sweep for every GMRES iteration. We implemented the ANNs and the optimal control method proposed here with the C++ interface of PyTorch [75], libtorch. PyTorch also supports parallelization with MPI, which is used throughout this work.

6.2. Domain truncation

In numerical simulations, wave propagation and other physical processes have to be truncated to bounded regions. To this end, we extend \mathcal{D} by a Perfectly Matched Layer (PML) on the right-hand side $\mathcal{D}_F = \mathcal{D} \cup \mathcal{D}_{\text{PML}}$. We only consider the 1D case where $\mathcal{D} = [0, L] \subset \mathbb{R}$ is a bounded and closed interval. The PML can be written as $\mathcal{D}_{\text{PML}} = (L, L_{\mathcal{D}_F}]$ with $L_{\text{PML}} := L_{\mathcal{D}_F} - L$. Inside the PML-region we have the problem

$$\partial_{tt}\mathbf{p} + \Gamma_0\partial_t\mathbf{p} + v_t^2\mathbf{p} - \kappa_x\varepsilon_\Delta v_t^2\mathbf{e} = 0 \quad \text{on } \mathcal{D}_{\text{PML}} \times I, \quad (6.1a)$$

$$\partial_t\mathbf{r} + \alpha_x\mathbf{r} - \varepsilon_\omega\sigma_x\mathbf{e} = 0 \quad \text{on } \mathcal{D}_{\text{PML}} \times I, \quad (6.1b)$$

$$\partial_t\mathbf{q} + \tilde{\alpha}_x\mathbf{q} - \tilde{\sigma}_x\partial_x\mathbf{e} = 0 \quad \text{on } \mathcal{D}_{\text{PML}} \times I, \quad (6.1c)$$

$$-\nabla \cdot \kappa_x^{-1}\nabla\mathbf{e} + \partial_x\mathbf{q} + \kappa_x\varepsilon_\omega\partial_{tt}\mathbf{e} + \kappa_x(\varepsilon_\Omega - \varepsilon_\omega)v_t^2\mathbf{e} - v_t^2P - \Gamma_0\partial_t\mathbf{p} + \partial_t(\varepsilon_\omega\sigma_x\mathbf{e} - \alpha_x\mathbf{r}) = 0 \quad \text{on } \mathcal{D}_{\text{PML}} \times I, \quad (6.1d)$$

$$\mathbf{e}(0) = 0 \quad \partial_t\mathbf{e}(0) = 0 \quad \text{on } \mathcal{D}_{\text{PML}}, \quad (6.1e)$$

$$\mathbf{e} = 0 \quad \text{on } \Gamma_D \cap \mathcal{D}_{\text{PML}} \times I. \quad (6.1f)$$

A more in-depth presentation with further discussion and references for PML can be found in [65].

6.3. Numerical convergence test of the space-time finite element method

Here we verify the numerical methods we developed for the forward problem. To this end we prescribe a function as the solution to the equations in Problem 2.1. We use the residual of this function as a source term, which in turn makes the prescribed function the solution. We use the Galerkin-collocation method proposed in Problem 2.2 for the time discretization and the finite element space \mathcal{V}_h defined in (3.2) for the spatial discretization. Consequently, we expect fourth-order convergence. We choose a 1D test case in the domain $\mathcal{D} = [0, 0.001955]$ over the time interval $I = [0, 1 \times 10^{-13}]$. As the electric field we choose

$$\mathbf{e}(x, t) = \sin(2\pi\omega_2(x - n_2t)) + \sin(2\pi\omega_1(x - n_1t)). \quad (6.2)$$

To compute the error in the physical domain and exclude error contributions from within the PML region, we introduce a weighting function $l: \mathcal{D} \rightarrow \mathbb{R}$ that is equal to one in the physical domain and zero in the PML region:

$$l(x) = \begin{cases} 0, & x \in \mathcal{D}_{\text{PML}}, \\ 1, & x \in \mathcal{D}. \end{cases}$$

Table 1: Calculated errors for the electric field \mathbf{e} and the auxiliary variable A for GCC¹(3).

k	$L^\infty - L^2(\mathbf{e})$	EOC	$L^\infty - L^2(A)$	EOC	$L^2 - L^2(\mathbf{e})$	EOC	$L^2 - L^2(A)$	EOC
τ_0	7.1334×10^{-1}	-	1.3573×10^4	-	2.2943×10^{-2}	-	4.0377×10^2	-
$\tau_0 \times 2^{-1}$	3.9379×10^{-2}	4.18	8.9722×10^2	3.92	1.3091×10^{-3}	4.13	3.0466×10^1	3.73
$\tau_0 \times 2^{-2}$	2.5447×10^{-3}	3.95	6.0263×10^1	3.90	8.3673×10^{-5}	3.97	2.0390	3.90
$\tau_0 \times 2^{-3}$	1.6050×10^{-4}	3.99	3.8358	3.97	5.2351×10^{-6}	4.00	1.2894×10^{-1}	3.98
$\tau_0 \times 2^{-4}$	1.0054×10^{-5}	4.00	2.4085×10^{-1}	3.99	3.2623×10^{-7}	4.00	8.0604×10^{-3}	4.00
$\tau_0 \times 2^{-5}$	6.2863×10^{-7}	4.00	1.5070×10^{-2}	4.00	2.0340×10^{-8}	4.00	5.0310×10^{-4}	4.00
$\tau_0 \times 2^{-6}$	3.9293×10^{-8}	4.00	9.4217×10^{-4}	4.00	1.2695×10^{-9}	4.00	3.1415×10^{-5}	4.00

Table 2: Calculated errors for the auxiliary variables P and U for GCC¹(3).

k	$L^\infty - L^2(U)$	EOC	$L^\infty - L^2(P)$	EOC	$L^2 - L^2(U)$	EOC	$L^2 - L^2(P)$	EOC
τ_0	1.2918	-	1.6725×10^{-3}	-	4.0207×10^{-2}	-	5.2300×10^{-5}	-
$\tau_0 \times 2^{-1}$	6.1522×10^{-2}	4.39	7.6061×10^{-5}	4.46	1.9033×10^{-3}	4.40	2.3583×10^{-6}	4.47
$\tau_0 \times 2^{-2}$	3.7217×10^{-3}	4.05	4.4730×10^{-6}	4.09	1.1401×10^{-4}	4.06	1.3805×10^{-7}	4.09
$\tau_0 \times 2^{-3}$	2.3102×10^{-4}	4.01	2.7585×10^{-7}	4.02	7.0556×10^{-6}	4.01	8.4946×10^{-9}	4.02
$\tau_0 \times 2^{-4}$	1.4416×10^{-5}	4.00	1.7193×10^{-8}	4.00	4.3980×10^{-7}	4.00	5.2888×10^{-10}	4.01
$\tau_0 \times 2^{-5}$	9.0060×10^{-7}	4.00	1.0741×10^{-9}	4.00	2.7465×10^{-8}	4.00	3.3023×10^{-11}	4.00
$\tau_0 \times 2^{-6}$	5.6281×10^{-8}	4.00	6.7133×10^{-11}	4.00	1.7160×10^{-9}	4.00	2.0634×10^{-12}	4.00

Furthermore we multiply l by the source term to restrict it to the physical domain. Thereby the solution inside D is given by (6.2). Then it propagates into D_{PML} where it is attenuated to the point of vanishing. We study the errors $e_z = \mathbf{z}(x, t) - \mathbf{z}_{\tau, h}(x, t)$ for $\mathbf{z} \in \{\mathbf{e}, \mathbf{a}, \mathbf{p}, \mathbf{u}\}$ in the norms

$$\|e_z\|_{L^\infty(L^2)} = \max_{t \in I} \left(\int_D |e_z|^2 dx \right)^{\frac{1}{2}} \quad \text{and} \quad \|e_z\|_{L^2(L^2)} = \left(\int_I \int_D |e_z|^2 dx dt \right)^{\frac{1}{2}}. \quad (6.3)$$

We abbreviate the error quantities $\|e_z\|_{L^\infty(L^2)}$ and $\|e_z\|_{L^2(L^2)}$ by $L^\infty\text{-}L^2(\mathbf{z})$ and $L^2\text{-}L^2(\mathbf{z})$ for $\mathbf{z} \in \{\mathbf{e}, \mathbf{a}, \mathbf{p}, \mathbf{u}\}$. The errors are calculated by simultaneous refinement in space and time. In Table 1 we observe the fourth order convergence in the variables \mathbf{e} and \mathbf{a} . For the auxiliary variables \mathbf{u} and \mathbf{p} we observe the same convergence rates in Table 2, which highlights the advantage of modelling these auxiliary variables with differential equations; cf. [65].

6.4. Test of the solution operator and optimal control methodology

In order to evaluate our algorithm, we construct an artificial test case similar to a numerical convergence test studied before. This test aims to provide empirical evidence of the algorithm's capability to solve complex problems. By this rigorous evaluation, we hope to gain insights into its strengths and weaknesses and identify optimal parametrizations that may be employed in the practical test case.

6.4.1. Training and testing of the solution operator

In a first step we construct a test for the solution operator, where we consider plane waves in vacuum. We generate the training data from plane waves at frequencies $f \in \{291.56 \text{ THz}, 290.56 \text{ THz}, 2 \cdot 291.56 \text{ THz}, 2 \cdot 290.56 \text{ THz}\}$. These frequencies are in the range of what we encounter in practice

for the THz generation. For the test we choose 2 plane waves with frequencies f_1, f_2 drawn from a continuous uniform distribution with support $(290.56 \text{ THz}, 2 \cdot 291.56 \text{ THz})$. Then we add two more plane waves by choosing the frequencies $f_3 = f_1 + 1 \text{ THz}$ and $f_4 = f_2 + 1 \text{ THz}$. We choose a 1D test case in the domain $\mathcal{D} = [0, 3 \times 10^{-14} c_0]$ over the time interval $I = [0, 1 \times 10^{-14}]$. The spatial domain has 3 periods with $\Lambda = 1 \times 10^{-14} c_0$. Therefore, the solution operator is always applied 3 times onto itself. This is done throughout this subsection.

We test FNOs and GRUs. Each of these models are trained and evaluated with varying numbers of layers and layer widths to evaluate their performances. In Table 3 we collect all configurations used here. For some of them, Fig. 4 shows the loss curves. The legend entries are named according to the rows and columns in Table 3. It is evident that although both models achieve the same level of accuracy, the GRU exhibits significant instability and oscillation in its loss. We attempted to address this issue by using an annealing learning rate during training and conducted extensive tuning of the hyperparameters, but the instability persisted. We note that one batch of training data used for Fig. 4 already contains 10 000 timesteps, so the issue could be related to the long term stability of the GRU. However, the prediction of 10000 timesteps is low compared to our practical example in the following section. The FNO on the other hand converges fast, especially for networks with 8 layers compared to the ones with 4 layers (cf. 4(a)). Due to the simplicity of the problem setting, the best models exhibit a similar loss across all architectures, eventhough the number of trainable parameters varies by multiple orders; cf. Table 3. Although the GRUs are smaller in these scenarios, the average training time is eight times longer for the same number of layers l and width w .

In order to show the advantage of the higher regularity time discretization, we use different loss functions during training. We consider the three loss functions

$$l_{C^1}^2(\mathbf{e}, \hat{\mathbf{e}}) = \left(\frac{1}{|I||\mathcal{D}|} \int_I \int_{\mathcal{D}} |\hat{\mathbf{e}} - \mathbf{e}|^2 dx dt \right), \quad (6.4a)$$

$$l_{\partial t}^2(\mathbf{e}, \hat{\mathbf{e}}) = \frac{1}{N} \sum_{i=1}^N |\hat{\mathbf{e}}_i - \mathbf{e}_i|^2 + \frac{1}{N} \sum_{i=1}^N |\partial_t \hat{\mathbf{e}}_i - \partial_t \mathbf{e}_i|^2, \quad (6.4b)$$

$$l^2(\mathbf{e}, \hat{\mathbf{e}}) = \frac{1}{N} \sum_{i=1}^N |\hat{\mathbf{e}}_i - \mathbf{e}_i|^2. \quad (6.4c)$$

Here l_{C^1} is motivated by the higher order time discretization and to evaluate the integrals we integrate the Hermite-type polynomials on the subintervals analytically. The second loss makes use of the data provided by the higher order time discretization but only considers the error in the collocation points (the subinterval endpoints). Since the losses themselves are difficult to compare, we study the errors $e_e = \hat{\mathbf{e}}(x, t) - \mathbf{e}(x, t)$ in the norms given in (6.3) with the abbreviations L^∞ - $L^2(\mathbf{e})$ and L^2 - $L^2(\mathbf{e})$. In Fig. 5, we evaluate the networks on successively refined time meshes in line with a numerical convergence test. For each refinement we use a new ANN which is trained as mentioned at the beginning of this section. The errors are then evaluated during the testing of the ANNs, which we also described above.

For the GRU the test results are stable, despite the high oscillations observed during the training time. Furthermore, all three loss functions lead to similar results. The GRUs do not benefit from the two loss functions which include the time derivative.

The FNO on the other hand profits from the added information and is otherwise stuck at high errors. Even at high time resolution, the network encounters difficulty in distinguishing frequencies that are just 1 THz apart. Including the time derivative via the loss functions (6.4a) or (6.4b) is important for effectively training the network. However, the difference between them is negligible. Interestingly we are able to observe linear convergence for both networks.

$l \setminus w$	4	8	16	32	$l \setminus w$	4	8	16	32
1	1317	2665	6993	22177	1	88	272	928	3392
2	1593	3761	11361	39617	2	208	704	2560	9728
4	2145	5953	20097	74497	4	448	1568	5824	22400
8	3249	10337	37569	144257	8	928	3296	12352	47744

Table 3: The number of parameters of the FNO (left) and GRU (right) for different parametrizations: The number of layers l and the width of the layers w .

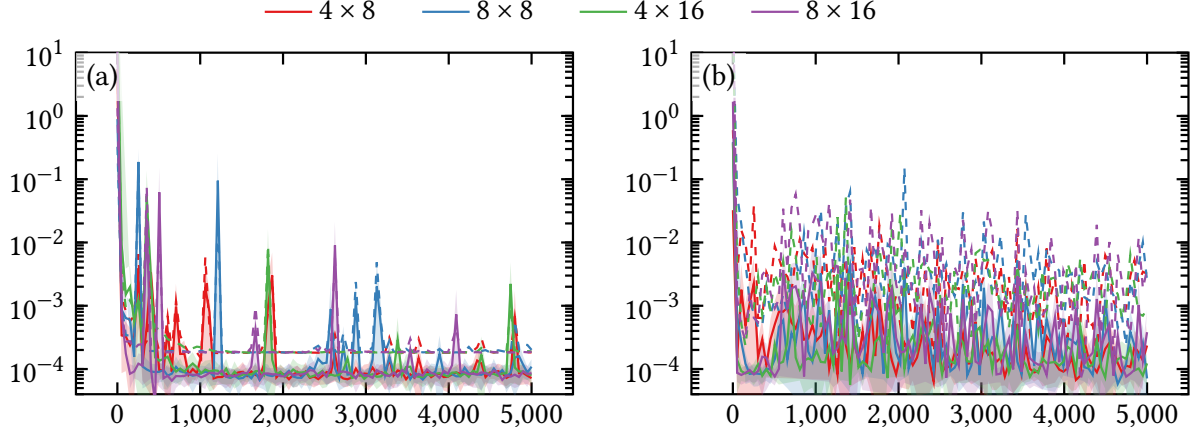


Figure 4: The average training (solid) and validation (dashed) loss ($l_{C_1}^2$, Eq. (6.4a)) for FNO (a) and GRU (b) architectures, smoothed with gnuplots smooth acsplines method. In order to avoid clutter and focus on the relevant results, we exclude larger network parametrizations that do not provide any additional accuracy benefits from the figure. The notation for the legend entries is $l \times w$, where l is the number of layers and w the layer width.

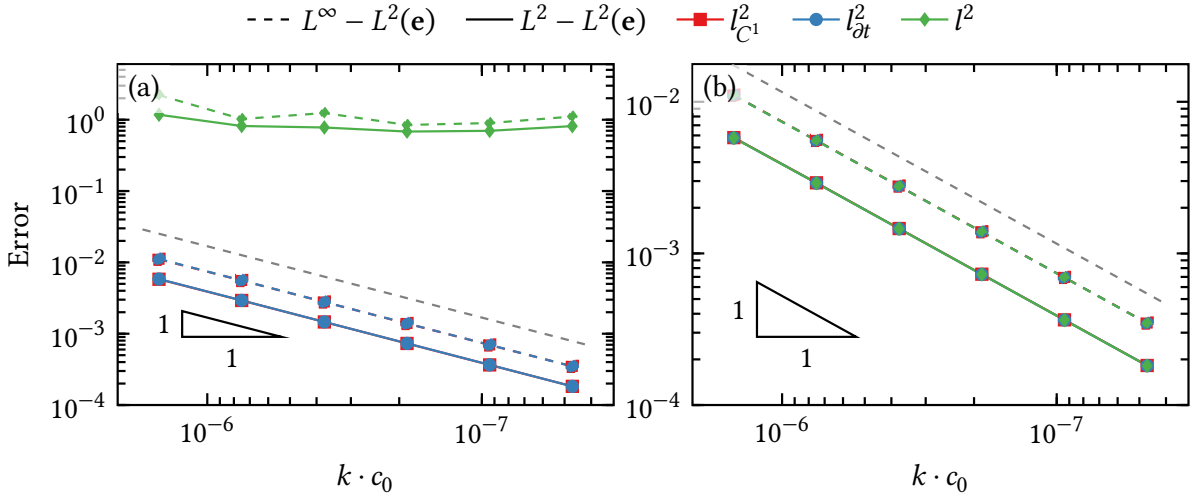


Figure 5: Convergence of the $L^\infty(L^2)$ (dashed) and $L^2(L^2)$ (solid) loss for FNO (a), GRU (b). The dashed grey line corresponds to linear convergence $O(n)$.

6.4.2. Computational efficiency of the solution operator

For the training of the ANNs, we implemented a distributed training algorithm similar to the one in [58]. In contrast to [58], we synchronize the network parameters by averaging them over all processes. For the available resources of 5 nodes, each with 2 GPUs, we are unable to determine any significant performance gains from considering only the neighboring MPI processes. Our distributed implementation is not equivalent to the sequential implementation due to the synchronization of the network parameters and not the gradients, which reduces the computational overhead. In the tests we run in this work, there is no disadvantage to this approach, yielding the same accuracies up to machine precision. In [58] the authors show that their decentralized algorithm, which is related to our approach, leads to the same convergence rate as the vanilla SGD.

Fig. 6 shows the strong scaling of the algorithm and the corresponding energy consumption for the two network architectures under consideration. The tests are run on an HPC cluster with 5 GPU nodes, each with 2 Nvidia A100 GPUs and 2 Intel Xeon Platinum 8360Y CPUs. The scaling tests are performed with 1 GPU as a baseline and with 1 to 5 nodes, always using both GPUs on the node. The number of MPI processes are equal to the number of GPUs such that one MPI process uses one GPU and CPU. We further note that, as shown in Table 4, the training and evaluation times are equal across one architecture, although the number of parameters differ significantly (cf. Table 3). However the implementation in PyTorch is optimized for larger networks and the ones we use are too small, to make a difference in computation times.

Fig. 6 and 7 (a) illustrate the near-optimal scaling performance for up to 4 GPUs. For 6 GPUs, the impact of synchronization costs becomes noticeable, as shown in Fig. 7 (a) and saturates afterwards. A further comparison of our implementation with the asynchronous implementation available only in PyTorch’s Python interface would require significant effort since we have exclusively used PyTorch’s C++ interface. Such a comparison for the assessment of our implementation is beyond the scope of this work. Here, we concentrate on evaluating the strong scaling test by means of the speedup S and energy ratio R ,

$$S = \frac{t_{\text{wall}}(1)}{t_{\text{wall}}(n)}, \quad (6.5a) \quad R = \frac{E(n)}{E(1)}, \quad (6.5b)$$

where n is the number of GPUs (which coincides with the number of MPI processes in this study), $E(n)$ is the energy consumed by the CPU, memory and GPU and t_{wall} is the wall clock time. The energy consumption of the CPU and memory is almost constant, with the increase in energy consumption primarily attributable to additional GPUs. Furthermore, the costs for CPU and memory are high and the energy consumption of the GPUs only became larger when using 10 GPUs. Overall our implementation exhibits great performance for this small artificial problem. This is confirmed by the productivity metric P in Fig. 7 (c), which is defined as the ratio of S and R , as per [3]. The optimal productivity lies at 6 GPUs and the results are promising for scaling to larger problems.

6.4.3. Optimal control through Deep Neural Networks

In order to test the methodology we propose in Section 5, we construct a simple OCP based on the solution operator we obtained in the last section. Initially, we sample 4 super Gaussian pulses parametrized as in (5.7a) and define Ξ from (5.7b) accordingly ($n = 4$). We choose a supergaussian pulse of order $p = 6$, a full-width half maximum of $\tau = 1 \times 10^{-14}$ s and the frequencies $f_1 = 291.56$ THz, $f_2 = 290.56$ THz, $f_3 = 2 \cdot 291.56$ THz, $f_4 = 2 \cdot 290.56$ THz. The time domain is chosen as $I = [-8 \times 10^{-15}, 8 \times 10^{-15}]$ and the spatial domain $D = [-8 \times 10^{-15}c_0, 8 \times 10^{-15}c_0]$. In Table 5 we list the

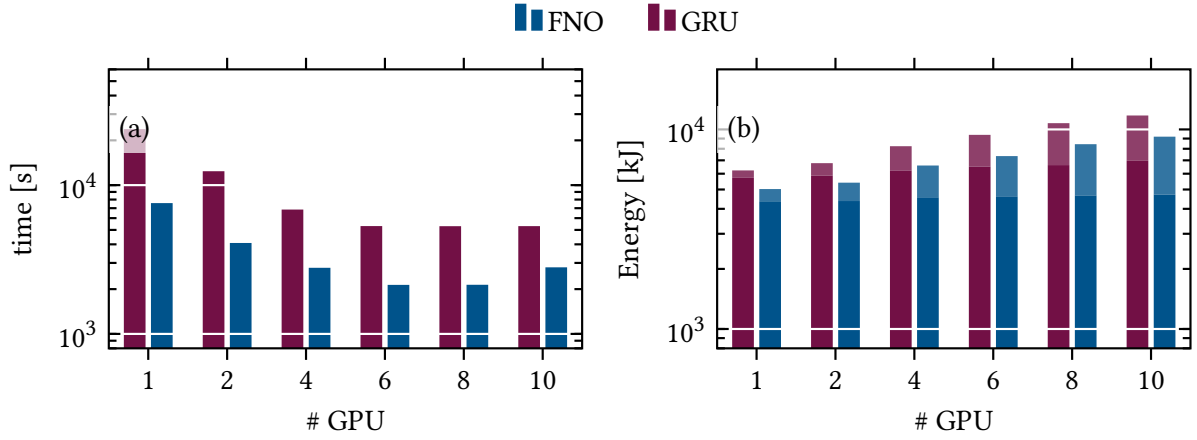


Figure 6: Runtime and energy consumption of GRUs and FNOs tested on up to 5 nodes of an HPC cluster with 2 NVidia A100 each. The tests were conducted with an FNO model of size (8×16) and a GRU of size (8×16) . The datasets are the largest presented in the solution operator tests.

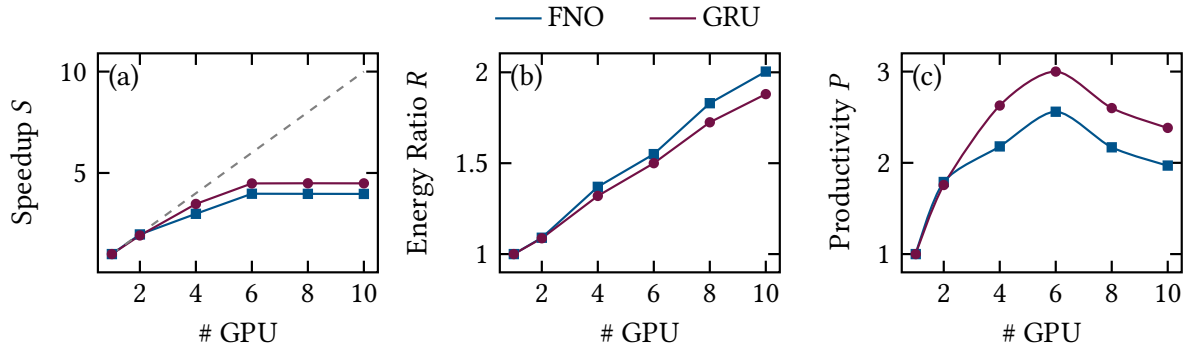


Figure 7: The speedup S , energy ratio R and productivity P calculated from the data of Fig. 6 for our scaling tests.

$l \setminus w$	8		16		$l \setminus w$	8		16	
	SO	OCP	SO	OCP		SO	OCP	SO	OCP
4	11 609	130.37	11 678	176.40	4	23 796	153.18	23 756	145.81
8	11 647	223.73	11 646	199.06	8	23 652	151.23	23 764	169.07

Table 4: The wall time for the different stages of our proposed method in seconds: the solution operator training (SO) and the solution of the OCP. The table on the left contains results for the FNO and the one on the right contains results for the GRU for different parametrizations: The number of layers l and the width of the layers w .

initial parameters $\xi_0 \in \Xi$ of the pulse (cf. Algorithm 5.1, line 1) for all tests performed in this section, except for $\varphi_1 = \varphi_2 = \varphi_3 = \varphi_4 = \zeta_1 = \zeta_2 = \zeta_3 = \zeta_4 = 0$, since they showed low sensitivity.

The setting for the OCP is described in Problem 5.2. We choose the cost function such that the amplitudes of the two high frequencies f_3, f_4 are minimized. To this end, we put $f_\Omega = \frac{1}{2}(f_3 + f_4)$ and $r = 10$ THz in (5.4). The solution to this minimization problem is trivial, as setting the amplitude of the two high frequencies to zero would be sufficient to solve the problem. For the ANNs exploiting the linearity is not straightforward: The solution operator has to generalize from plane waves to Gaussian pulses and is a nonlinear operator by construction. Therefore, linearity has to be learned from the training data, and we cannot assume that we always achieve that.

We compare two different optimization methods: the AdamW optimizer [50], a modified version of stochastic gradient descent, and the L-BFGS [59], a quasi-Newton method. In Fig. 8 we plot the development of the amplitudes and cost function over the epochs. The first row of plots contains the results for the FNOs. The L-BFGS method converges in 1 step and only changes slightly afterwards. However, the two optimization routines don't lead to the same result. The L-BFGS gets stuck in the first local minimum it finds, the AdamW optimizer does not due to the added momentum. We can rule out the penalty parameter as the reason. We set it to $\beta = 6 \times 10^{-14}$ in all of our tests. Slight differences of other parameters introduced during the optimization and differences in the output of the ANN are further contributing factors. In Table 5 we compare the final pulse parametrizations and the cost function of the OCP for different networks using the AdamW optimizer. All parameters of the pulse are subject to optimization and can be affected by updates during optimization. For the FNO, the amplitude a_1 is correctly used as the main quantity to control the optimization and other parameters show low sensitivity. The results for the FNO are independent of the parametrization and reach nearly the same values with respect to the parameters.

The second row of plots in Fig. 8 contains the results for the GRUs in solving the OCP. The L-BFGS optimizer stagnates and fails to improve the cost function, while the AdamW optimizer shows some improvements. However, the solution operator resulting from the GRUs can't distinguish between different frequencies. In Table 5 we observe that the GRUs nearly remove all the lower frequencies. In the previous section the accuracy and convergence behavior of the GRU and FNO were almost the same. From the unsatisfactory results for the solution of the OCP with GRUs we conclude that the GRU architecture is not well-suited for this type of problem. Furthermore, the applicability of the ANNs to Problem 5.2 is predicted by the ability to approximate the solution operator \mathcal{S} , which is difficult to evaluate experimentally. Nevertheless, FNOs are promising tools for this task based on their performance in our experiments. Overall the FNOs solve the test problem and are good candidates for the deployment to the realistic problem from nonlinear optics.

6.4.4. Computational efficiency of the optimal control algorithm

For the evaluation of the ANN in our optimal control algorithm we only use one GPU on a single node, since the distributed algorithm does not pay off in that case due to the fast evaluation of the ANN. In Table 4 we show the wall times for the training of the solution operator and the wall time for the solution of the OCP. The wall time for the OCP is significantly lower than the training of the solution operator. The low cost of solving the OCP we is a considerable advantage, since we expect to reuse the trained solution operator multiple times in the optimal control setting. Overall, the approach has great potential for the solution of OCPs, since classical numerical solutions, even in this artificial settings, exhibit high computational cost. In the next section, we use highly accurate simulation data from a realistic physical setting to train the solution operator and apply it to Problem ref:problem:opconTHz, the OCP of maximizing THz generation.

Parametrization	τ [s]	P_1	a_1	f_1 [THz]	P_3	a_3	f_3 [THz]	J
Initial values	1.0×10^{-14}	6	1	291.56	6	1	$2 \cdot 291.56$	0
GRU, 4×8	9.9×10^{-13}	5.99	0.02654	291.56	5.99	0	$2 \cdot 291.56$	1.704×10^{-4}
GRU, 8×8	9.9×10^{-13}	5.99	0.02654	291.56	5.99	0	$2 \cdot 291.56$	1.741×10^{-4}
GRU, 4×16	9.9×10^{-13}	5.99	0.02654	291.56	5.99	0	$2 \cdot 291.56$	1.693×10^{-4}
GRU, 8×16	9.9×10^{-13}	5.99	0.02654	291.56	5.99	0	$2 \cdot 291.56$	1.740×10^{-4}
FNO, 4×8	9.9×10^{-13}	5.99	2.8339	291.56	5.99	0	$2 \cdot 291.56$	5.318×10^{-6}
FNO, 8×8	9.9×10^{-13}	5.99	2.8338	291.56	5.99	0	$2 \cdot 291.56$	5.276×10^{-6}
FNO, 4×16	9.9×10^{-13}	5.99	2.8339	291.56	5.99	0	$2 \cdot 291.56$	5.101×10^{-6}
FNO, 8×16	9.9×10^{-13}	5.99	2.8337	291.56	5.99	0	$2 \cdot 291.56$	5.105×10^{-6}

Table 5: The results for the test of the optimal control problem for different parametrizations of GRUs and FNOs after the training has converged. We show the parameters of 2 of the 4 pulses. All the parameters are trainable and therefore possibly affected by the updates during the optimization.

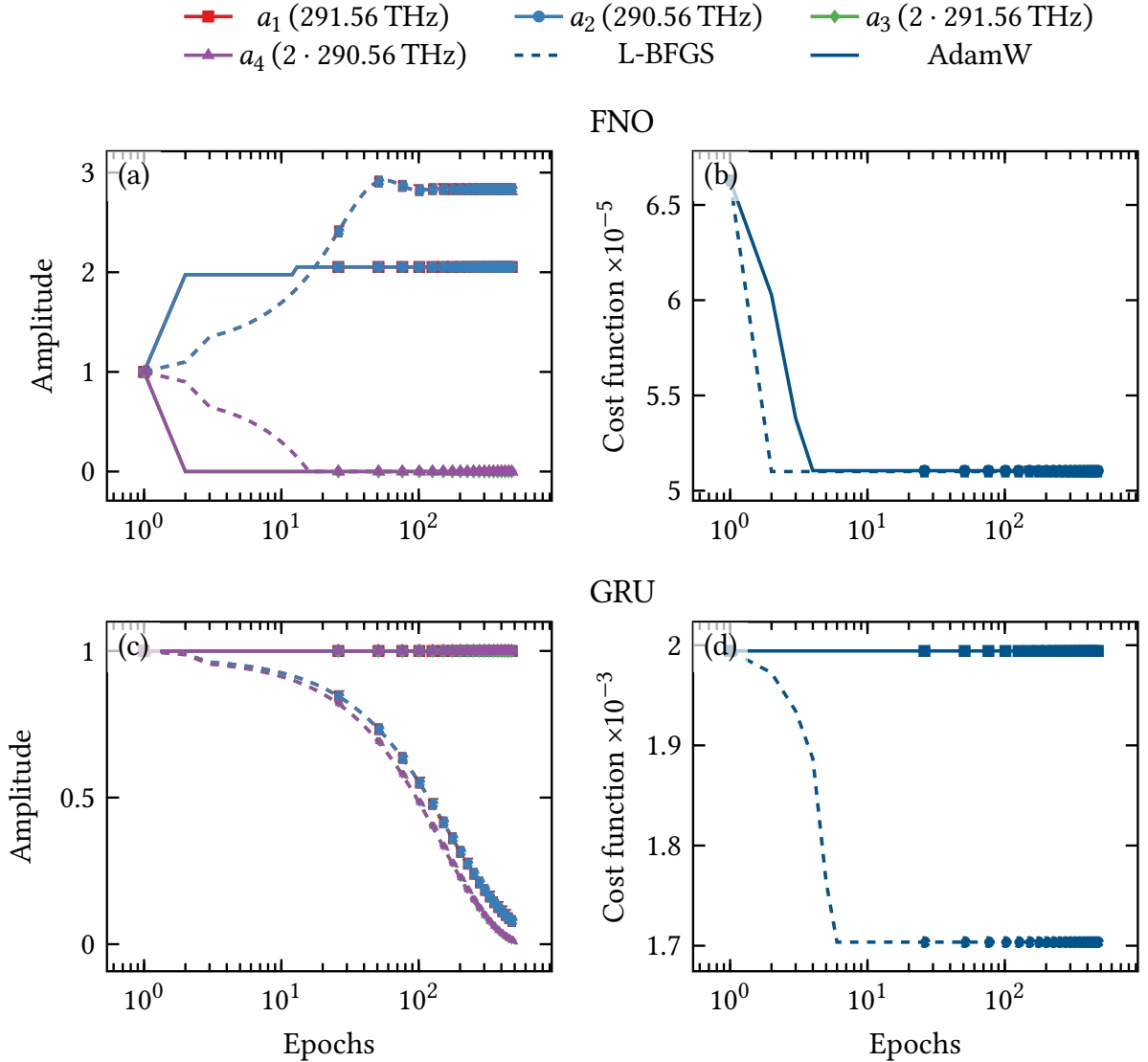


Figure 8: The evolution of the amplitudes of the pulses (a, c) and the cost function (b, d) for FNOs (the first row of the subplots) and GRUs (the second row of the subplots). Solid lines correspond to the optimization with L-BFGS and dashed lines to the AdamW optimizer.

6.5. THz Generation in a Periodically Poled Nonlinear Crystal

The main goal in this section is to show the potential of our proposed method by applying it to a case where experimental results are available [72], in order to verify that the algorithm solves an OCP in realistic settings. That potentially leads to the improvement of the experimental setup especially for higher intensities where simplified models fail. As in [65], we use 2 super Gaussian pulses parametrized as in (5.7a) and define Ξ from (5.7b) accordingly ($n = 2$). We choose a supergaussian pulse of order $p = 6$, a full-width half maximum of $\tau = 250$ ps and the frequencies $f_1 = 291.56$ THz, $f_2 = 291.26$ THz. The pulses are separated in center frequency by the THz frequency $f_\Omega = 0.3$ THz. In this section we choose a pulse with average fluence of 200 mJ cm^{-2} . The average fluence F is defined as the mean of the optical intensity I_e over time. The detailed definitions are given in Appendix C. In the simplified 1D case, they can be expressed as

$$I_e = \frac{1}{2} \varepsilon_0 c_0 |\sqrt{\varepsilon_r} * \mathbf{e}|^2, \quad (6.6a) \quad F = \frac{1}{T} \int_0^T I_e(t) dt, \quad (6.6b)$$

The pulse is applied at the left-hand side of the crystal by a Dirichlet boundary condition on Γ_{in} (cf. Fig. 3), propagates through the domain and enters the PML where it is attenuated. The problem setting is already sketched in Fig. 3. The computational effort for these simulations is high: The simulations presented here took 15 days on an HPC cluster using 5 nodes, each with 2 Intel Xeon Platinum 8360Y CPUs. In this study, we limited our investigations and numerical simulations to one spatial dimension. This was necessitated by simulation times and the added complexity of using PMLs in 2D and 3D. In the settings investigated here, the simplification of reducing the simulations to one spatial dimension and neglecting the impacts of the remaining spatial directions is not expected to significantly perturb the results. The simulation results presented here are based on a timestep size of $k = 5 \times 10^{-17}$ and average cell-size of 5.175×10^{-8} , which leads to 5×10^9 number of timesteps and 1 703 940 degrees of freedom in space.

6.5.1. Training and Evaluation of the Solution Operator

As in the case of artificial data in Section 6.4.3, the simulation data is used to train a solution operator. We test only FNOs, since GRUs did not show satisfactory results in the artificial test case. Fig. 9(a) shows the losses of some parametrizations given in Table 3. For the training we split the data set obtained in the setting described above into a training and validation set. We simulate 25 periods of the crystal, where the first 15 periods are used for training and the last 10 periods are used for the validation.

In Fig. 9(a) we observe fast convergence of the FNOs, even with larger architectures, and the best models exhibit a similar loss across all architectures. We use the two loss functions (6.4a) and (6.4b), since the added information of the time derivative proved to be essential for good performance in the settings we investigate in this work. In Fig. 9(b) we plot the errors $e = \mathbf{e}_{\text{GCC}^1(3)} - \mathbf{e}_{\text{FNO}}$. For different timestep-sizes we use different FNOs, trained on simulation data obtained with the same step size. We observe linear convergence as before in the artificial test case.

We test the FNO on pulses $g(t) \in \mathcal{P}[\Xi]$ with different average fluence 100 mJ cm^{-2} , 200 mJ cm^{-2} , 300 mJ cm^{-2} , 400 mJ cm^{-2} , 500 mJ cm^{-2} and 600 mJ cm^{-2} . Other parameters remain unchanged compared to the training scenario. We test the different parametrizations of the FNOs (cf. Table 3). We evaluate the accuracy of the FNOs based on the internal conversion efficiency (CE) and the errors (6.3). In Fig. 10(a), we compare the CE obtained from the FNO simulations with numerical simulations obtained from the space-time finite element method presented here and experimental results from [72].

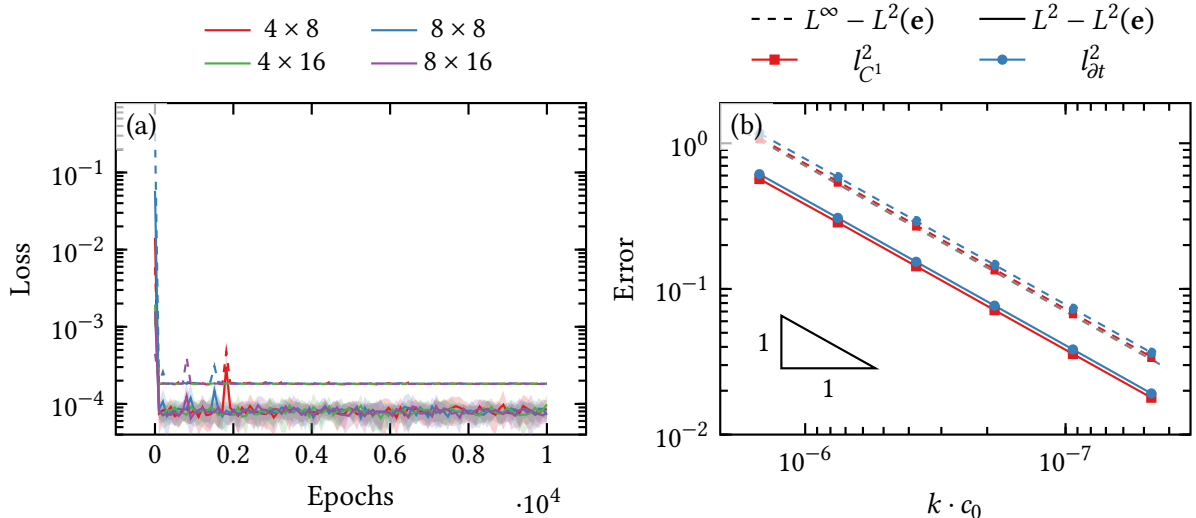


Figure 9: The average training (solid) and validation (dashed) loss for the FNO architecture (a). The right subplot (b) shows the convergence of the $L^\infty(L^2)$ (dashed) and $L^2(L^2)$ (solid) error for FNO.

The numerical simulations and FNOs are in good agreement with the experimental data and are mostly close or within the standard deviation of the experimental data. The FNOs perform very well, but lose some accuracy as the fluence increases. This is expected, since we only trained it with data from simulations with a fluence of 200 mJ cm^{-2} . Nevertheless, they seem to learn the physical processes governing the THz generation accurately.

We analyze the accuracy of the FNO further in Fig. 10 (b), where we plot the errors $e = \mathbf{e}_{\text{GCC}^1(3)} - \mathbf{e}_{\text{FNO}}$, evaluated in the norms (6.3) for different values of the average fluence. Although the error grows with increasing fluence, for that the network was not trained, the results are promising. The FNO is able to provide a good generalization to pulses with higher fluence.

6.5.2. Optimal control through the Solution Operator

As the final task, we consider the Problem 5.2 in the realistic setting and compare the results to experimental results. In this case we want to maximize the radiation at the frequency $f_{\text{THz}} = 0.3 \text{ THz}$. Therefore, we set $f_\Omega = f_{\text{THz}}$ and $r = 0.25 \text{ THz}$ in (5.4). We test the method on the FNOs we trained in Section 6.5.1. Fig. 9 shows the losses on a subset of the parametrizations given in Table 3. The initial parameters correspond to the case we considered in Section 6.5.1 for an average fluence of 100 mJ cm^{-2} . As observed in 10 (a) the internal CE grows with increasing fluence. In order to maximize the 0.3 THz-frequency radiation the simplest improvement is an increase of the amplitude of the pulse. We test here if this gets picked up by the FNO and it successfully optimizes the internal CE. The internal CE is closely linked to the cost function of the OCP, which is proportional to the intensity at 0.3 THz.

Comparing AdamW optimizer and L-BFGS for optimization methods, we plot the amplitudes and cost function development over epochs in Fig. 11 (a), (b). Although the convergence is slower than the artificial test case, the trajectories are overall similar. Again, L-BFGS converges significantly faster than AdamW. Both reach similar optima, further improvement may be limited by the regularization term. Lowering it beyond the value we used before, lead to instabilities and implausible results. The reason for the slower convergence of the L-BFGS method is the requirement of using a lower learning-

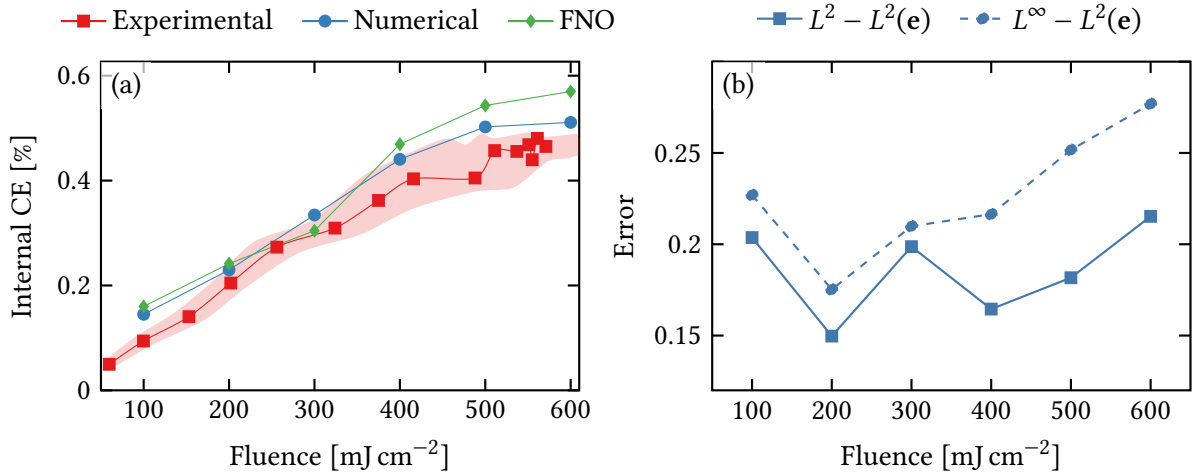


Figure 10: The left subplot shows the optical to THz conversion efficiency of the FNOs, simulation data and the experimental data from [72]. For the experimental data we calculate an envelope from the standard deviation, that reflects the measurement inaccuracies. The right subplot shows the errors between FNOs and numerical solution.

rate. Any attempt to use a higher learning-rate result in stagnation.

The second row of plots in Fig. 11 contains the internal optical to THz CE and the internal CE of the second harmonic generation. The optical to THz CE in Fig. 11 (c) grows proportionally to the cost function, which confirms that the FNO approximates at least a part of the solution operator and physical model. In order to improve the internal CE, the amplitude grows significantly, which confirms our expectation, that the amplitude should be the main tuning parameter. We also observe this in Table 6.

In good agreement to our previous observations in [65], the CE of the second harmonic generation in Fig. 11 (d) oscillates strongly. The reason for the oscillations is the phase-mismatch, which leads to oscillating negative and positive interference. This leads to varying conversion efficiencies over the layers, depending on how close we are to a phase-match. In Table 6, we compare the final pulse parametrizations and the cost function of the OCP for different networks using the AdamW optimizer. Overall, FNOs perform well for the optimization of optical to THz generation.

Performing the numerical simulations for obtaining the training data is the main contributor to the computational costs. The subsequent training of the solution operator takes 1 day and the final solution of the optimal control algorithm takes 2 hours at most. Considering that a single numerical solution takes 15 days, the proposed approach offers great potential for optimal control problems involving complex physics, in particular nonlinear optics. These problems are still computationally challenging and oftentimes remain infeasible through classical methods.

Parametrization	τ [ps]	P_1	a_1	f_1 [THz]	P_2	a_2	f_2 [THz]	\mathcal{J}	F [mJ cm ⁻²]
Initial values	250	6	1	291.26	6	1	291.56	0	100
FNO, 4 × 8	257.268	6.57	3.7140	291.26	6.56	3.7080	291.56	2.932×10 ³	402
FNO, 8 × 8	256.315	6.56	3.7257	291.26	6.56	3.6919	291.56	3.266×10 ³	402
FNO, 4 × 16	306.852	6.59	3.7284	291.26	6.63	3.7332	291.56	2.552×10 ³	403
FNO, 8 × 16	306.815	6.70	3.8010	291.26	6.71	3.7541	291.56	3.301×10 ³	406

Table 6: The results for the test of the OCP for different parametrizations of FNOs after the training has converged. We show the relevant parameters of the pulses. The amplitude is normalized w. r. t. the initial value. The fluence F is displayed in the last column.

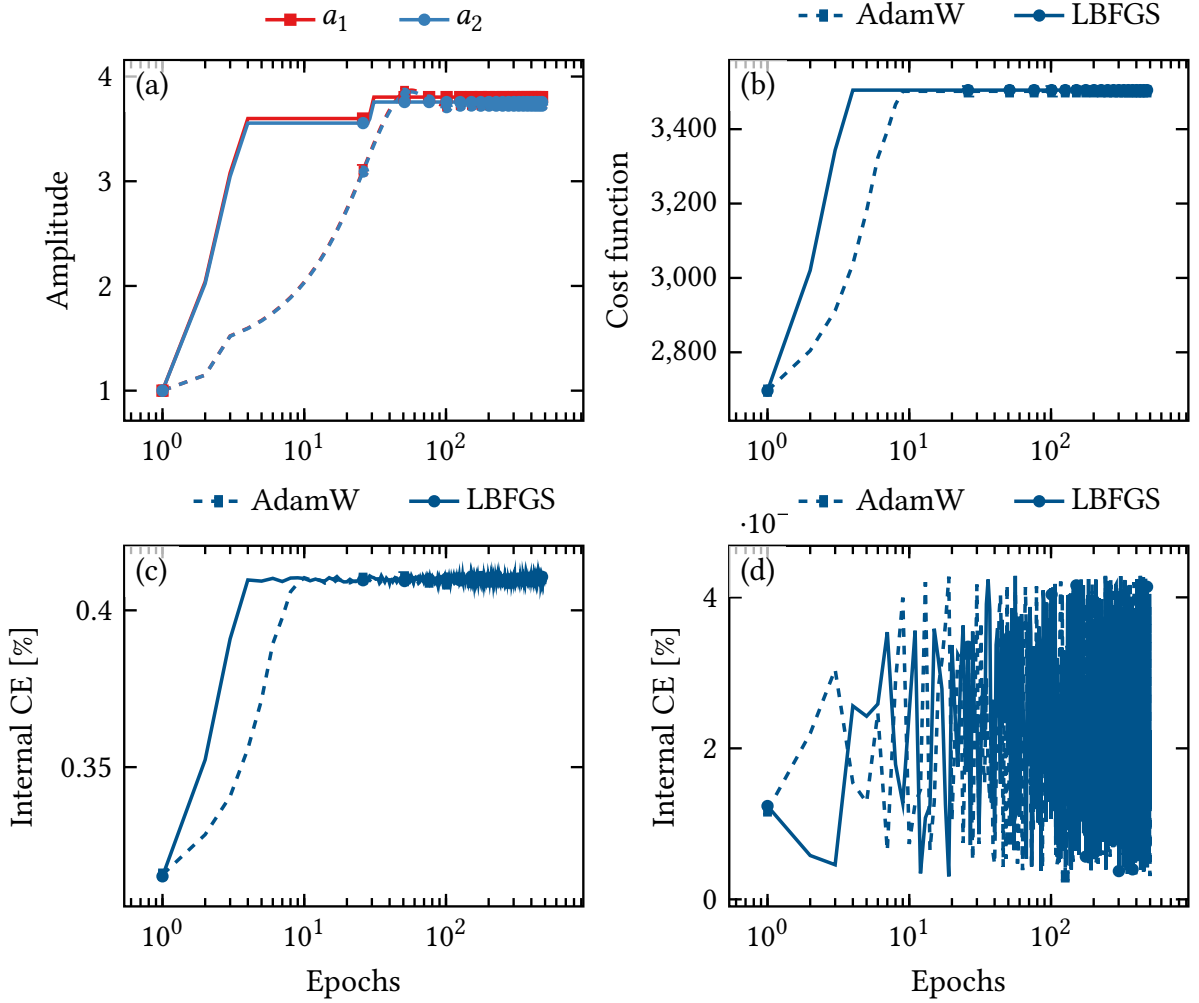


Figure 11: The evolution of the amplitudes of the pulse (a). The Subplot (b) shows the evolution of the cost function, (c) the internal optical-to-THz CE and (d) internal CE for the second harmonic.

Conclusion

In this paper we developed methods to solve an optimal control problem arising in nonlinear optics. To this end, we extended the Galerkin-collocation time discretization to a nonlinear dispersive wave equation. We observed that the method is particularly well suited for problems arising in nonlinear optics. We confirmed the results found in [4] by convergence tests. Although the implementation of the method is parallelized and able to run on HPC platforms, the solution time for using them within an optimal control loop is still too high.

We devised an algorithm which uses the simulation data with discrete solutions of higher regularity in time to train an ANN, which is used for the forward solve. The algorithm is applicable to a general optimal Dirichlet boundary control problem and can be extended to other optimal control problems. Our method allows for efficient solution of the optimal control problem, since we only require the solution at some collocation points, and don't need the full space-time solution. We compared GRUs and FNOs and tested their implementation on HPC platforms and verified it by a strong scaling test. We also evaluated the energy efficiency. We were able to observe first order convergence, which we only reached for the FNO with the added higher regularity. A thorough investigation of this phenomenon is subject to future work. The GRU architecture was not able to solve the optimal control problem satisfactorily despite its good accuracy during the initial tests. FNOs were successful in solving the optimal control problem. They clearly had an advantage over GRUs, since they are designed for solving PDEs.

The optical to THz conversion efficiency achieved by the FNOs was found to be in good agreement with experimental data. Moreover, the FNOs were successful in optimizing the efficiency of this conversion process in an optimal boundary control setting. Solving the whole optimal control problem with the trained solution operator is 360 times faster than a single forward solve with the numerical methods. Through its computational efficiency, the FNO has the potential to enable breakthroughs in the development of high-field THz pulses, by efficiently solving the optimization problem of maximizing the optical to THz conversion efficiency. The rapid convergence of the training and fast evaluation of the FNOs make them a cost-effective solution for this purpose and potentially other complex physical problems.

Acknowledgement

NM acknowledges support by the Helmholtz-Gesellschaft grant number HIDSS-0002 DASHH. Computational resources (HPC-cluster HSUper) were provided by the project hpc.bw, funded by dtec.bw – Digitalization and Technology Research Center of the Bundeswehr. FXK acknowledges support through ERC Synergy Grant (609920).

References

- [1] David S. Abraham and Dennis D. Giannacopoulos. “A Convolution-Free Mixed Finite-Element Time-Domain Method for General Nonlinear Dispersive Media”. In: *IEEE Transactions on Antennas and Propagation* 67.1 (Jan. 2019), pp. 324–334. ISSN: 1558-2221. DOI: 10.1109/TAP.2018.2874798.
- [2] Mathias Anselmann and Markus Bause. “Numerical Study of Galerkin–Collocation Approximation in Time for the Wave Equation”. In: *Mathematics of Wave Phenomena*. Ed. by Willy Dörfler et al. Cham: Springer International Publishing, 2020, pp. 15–36. ISBN: 978-3-030-47173-6 978-3-030-47174-3. DOI: 10.1007/978-3-030-47174-3_2.

- [3] Mathias Anselmann et al. *An Energy-Efficient GMRES-Multigrid Solver for Space-Time Finite Element Computation of Dynamic Poro- and Thermoelasticity*. Mar. 12, 2023. DOI: 10.48550/arXiv.2303.06742. arXiv: 2303.06742 [cs, math]. preprint.
- [4] Mathias Anselmann et al. “Galerkin–Collocation Approximation in Time for the Wave Equation and Its Post-Processing”. In: *ESAIM: Mathematical Modelling and Numerical Analysis* 54.6 (6 Nov. 1, 2020), pp. 2099–2123. ISSN: 0764-583X, 1290-3841. DOI: 10.1051/m2an/2020033.
- [5] Harbir Antil, Hugo Díaz, and Evelyn Herberg. *An Optimal Time Variable Learning Framework for Deep Neural Networks*. Apr. 18, 2022. arXiv: 2204.08528 [cs, math]. URL: <http://arxiv.org/abs/2204.08528>. preprint.
- [6] Daniel Arndt et al. “The Deal.II Library, Version 9.3”. In: *Journal of Numerical Mathematics* 29.3 (Sept. 1, 2021), pp. 171–186. ISSN: 1569-3953. DOI: 10.1515/jnma-2021-0081.
- [7] W. Bangerth, M. Geiger, and R. Rannacher. “Adaptive Galerkin Finite Element Methods for the Wave Equation”. In: *Comp. Meth. Appl. Math.* 10 (2010), pp. 3–48. DOI: 10.2478/cmam-2010-0001.
- [8] Lehel Banjai, Emmanuil H. Georgoulis, and Oluwaseun Lijoka. “A Trefftz Polynomial Space-Time Discontinuous Galerkin Method for the Second Order Wave Equation”. In: *SIAM Journal on Numerical Analysis* 55.1 (Jan. 2017), pp. 63–86. ISSN: 0036-1429. DOI: 10.1137/16M1065744.
- [9] Markus Bause, Marius Paul Bruchhäuser, and Uwe Köcher. “Flexible Goal-Oriented Adaptivity for Higher-Order Space-Time Discretizations of Transport Problems with Coupled Flow”. In: *Computers & Mathematics with Applications* 91 (June 2021), pp. 17–35. ISSN: 08981221. DOI: 10.1016/j.camwa.2020.08.028. arXiv: 2002.06855.
- [10] Simon Becher and Gunar Matthies. “Variational Time Discretizations of Higher Order and Higher Regularity”. In: *BIT Numerical Mathematics* 61.3 (Sept. 1, 2021), pp. 721–755. ISSN: 1572-9125. DOI: 10.1007/s10543-021-00851-6.
- [11] Martin Benning et al. “Deep Learning as Optimal Control Problems: Models and Numerical Methods”. In: *Journal of Computational Dynamics* 6.2 (2019), pp. 171–198. ISSN: 2158-2491. DOI: 10.3934/jcd.2019009.
- [12] Alain Bensoussan et al. “Chapter 16 - Machine Learning and Control Theory”. In: *Handbook of Numerical Analysis*. Ed. by Emmanuel Trélat and Enrique Zuazua. Vol. 23. Numerical Control: Part A. Elsevier, Jan. 1, 2022, pp. 531–558. DOI: 10.1016/bs.hna.2021.12.016.
- [13] Luc Berger-Vergiat et al. *MueLu User’s Guide*. SAND2019-0537. Sandia National Laboratories, 2019.
- [14] Kaushik Bhattacharya et al. “Model Reduction And Neural Networks For Parametric PDEs”. In: *The SMAI Journal of computational mathematics* 7 (2021), pp. 121–157. ISSN: 2426-8399. DOI: 10.5802/smai-jcm.74.
- [15] Robert W. Boyd. “Chapter 1 - The Nonlinear Optical Susceptibility”. In: *Nonlinear Optics (Fourth Edition)*. Ed. by Robert W. Boyd. Academic Press, Jan. 1, 2020, pp. 1–64. ISBN: 978-0-12-811002-7. DOI: 10.1016/B978-0-12-811002-7.00010-2.
- [16] Marius Paul Bruchhäuser. “Goal-Oriented Space-Time Adaptivity for a Multirate Approach to Coupled Flow and Transport”. Thesis. Universitätsbibliothek der HSU / UniBwH, July 2022. DOI: 10.24405/14380.

- [17] René Carmona and Mathieu Laurière. “Convergence Analysis of Machine Learning Algorithms for the Numerical Solution of Mean Field Control and Games I: The Ergodic Case”. In: *SIAM Journal on Numerical Analysis* 59.3 (Jan. 2021), pp. 1455–1485. ISSN: 0036-1429. DOI: 10.1137/19M1274377.
- [18] René Carmona and Mathieu Laurière. *Convergence Analysis of Machine Learning Algorithms for the Numerical Solution of Mean Field Control and Games: II – The Finite Horizon Case*. Mar. 29, 2021. DOI: 10.48550/arXiv.1908.01613. arXiv: 1908.01613 [cs, math]. preprint.
- [19] Tianping Chen and Hong Chen. “Universal Approximation to Nonlinear Operators by Neural Networks with Arbitrary Activation Functions and Its Application to Dynamical Systems”. In: *IEEE Transactions on Neural Networks* 6.4 (1995), pp. 911–917. DOI: 10.1109/72.392253.
- [20] Zhengdao Chen et al. “Symplectic Recurrent Neural Networks”. In: Eighth International Conference on Learning Representations. Apr. 2020. URL: https://iclr.cc/virtual_2020/poster_BkgYPREtPr.html#details.
- [21] K. Cho et al. “Learning Phrase Representations Using RNN Encoder-Decoder for Statistical Machine Translation”. In: *Conference on Empirical Methods in Natural Language Processing (EMNLP 2014)*. 2014. DOI: 10.3115/v1/D14-1179.
- [22] Salvatore Cuomo et al. “Scientific Machine Learning Through Physics-Informed Neural Networks: Where We Are and What’s Next”. In: *Journal of Scientific Computing* 92.3 (July 26, 2022), p. 88. ISSN: 1573-7691. DOI: 10.1007/s10915-022-01939-z.
- [23] R. Dautray et al. *Mathematical Analysis and Numerical Methods for Science and Technology: Volume 5 Evolution Problems I*. Mathematical Analysis and Numerical Methods for Science and Technology. Springer Berlin Heidelberg, 1999. ISBN: 978-3-540-66101-6.
- [24] Willy Dörfler, Stefan Findeisen, and Christian Wieners. “Space-Time Discontinuous Galerkin Discretizations for Linear First-Order Hyperbolic Evolution Systems”. In: *Computational Methods in Applied Mathematics* 16.3 (July 1, 2016), pp. 409–428. ISSN: 1609-9389. DOI: 10.1515/cmam-2016-0015.
- [25] Willy Dörfler et al. “2. Parallel Adaptive Discontinuous Galerkin Discretizations in Space and Time for Linear Elastic and Acoustic Waves”. In: *2. Parallel Adaptive Discontinuous Galerkin Discretizations in Space and Time for Linear Elastic and Acoustic Waves*. De Gruyter, Sept. 23, 2019, pp. 61–88. ISBN: 978-3-11-054848-8. DOI: 10.1515/9783110548488-002.
- [26] Weinan E. “A Proposal on Machine Learning via Dynamical Systems”. In: *Communications in Mathematics and Statistics* 5.1 (Mar. 1, 2017), pp. 1–11. ISSN: 2194-671X. DOI: 10.1007/s40304-017-0103-z.
- [27] Weinan E, Jiequn Han, and Qianxiao Li. “A Mean-Field Optimal Control Formulation of Deep Learning”. In: *Research in the Mathematical Sciences* 6.1 (Mar. 2019), p. 10. ISSN: 2522-0144, 2197-9847. DOI: 10.1007/s40687-018-0172-y.
- [28] Weinan E and Bing Yu. “The Deep Ritz Method: A Deep Learning-Based Numerical Algorithm for Solving Variational Problems”. In: *Communications in Mathematics and Statistics* (Mar. 1, 2018). ISSN: 2194-6701. DOI: 10.1007/s40304-018-0127-z.
- [29] L. C. Evans. *Partial Differential Equations*. Graduate Studies in Mathematics. American Mathematical Society, 2010.

- [30] Yuwei Fan, Cindy Orozco Bohorquez, and Lexing Ying. “BCR-Net: A Neural Network Based on the Nonstandard Wavelet Form”. In: *Journal of Computational Physics* 384 (2019), pp. 1–15. DOI: 10.1016/j.jcp.2019.02.002.
- [31] Yuwei Fan et al. “A Multiscale Neural Network Based on Hierarchical Matrices”. In: *Multiscale Modeling & Simulation* 17.4 (2019), pp. 1189–1213. DOI: 10.1137/18m1203602.
- [32] Stefan Matthias Findeisen. *A Parallel and Adaptive Space-Time Method for Maxwell’s Equations*. 2016. DOI: 10.5445/IR/1000056876.
- [33] Stefania Fresca and Andrea Manzoni. “POD-DL-ROM: Enhancing Deep Learning-Based Reduced Order Models for Nonlinear Parametrized PDEs by Proper Orthogonal Decomposition”. In: *Computer Methods in Applied Mechanics and Engineering* 388 (2022), pp. 114–181. DOI: 10.1016/j.cma.2021.114181.
- [34] Craig Gin et al. “Deep Learning Models for Global Coordinate Transformations That Linearize PDEs”. In: *European Journal of Applied Mathematics* (Sept. 24, 2020), pp. 1–25. ISSN: 0956-7925, 1469-4425. DOI: 10.1017/S0956792520000327. arXiv: 1911.02710.
- [35] J. Gopalakrishnan, J. Schöberl, and C. Wintersteiger. “Mapped Tent Pitching Schemes for Hyperbolic Systems”. In: *SIAM Journal on Scientific Computing* 39.6 (Jan. 2017), B1043–B1063. ISSN: 1064-8275. DOI: 10.1137/16M1101374.
- [36] Loukas Grafakos. *Classical Fourier Analysis*. Vol. 249. Graduate Texts in Mathematics. New York, NY: Springer, 2014. ISBN: 978-1-4939-1193-6 978-1-4939-1194-3. DOI: 10.1007/978-1-4939-1194-3.
- [37] Tamara G. Grossmann et al. *Can Physics-Informed Neural Networks Beat the Finite Element Method?* Feb. 8, 2023. DOI: 10.48550/arXiv.2302.04107. arXiv: 2302.04107 [cs, math]. preprint.
- [38] Martin Gugat. *Optimal Boundary Control and Boundary Stabilization of Hyperbolic Systems*. SpringerBriefs in Electrical and Computer Engineering. Cham: Springer International Publishing, 2015. ISBN: 978-3-319-18889-8 978-3-319-18890-4. DOI: 10.1007/978-3-319-18890-4.
- [39] Eldad Haber and Lars Ruthotto. “Stable Architectures for Deep Neural Networks”. In: *Inverse Problems. An International Journal on the Theory and Practice of Inverse Problems, Inverse Methods and Computerized Inversion of Data* 34.1 (2017), p. 014004.
- [40] Quercus Hernández et al. “Structure-Preserving Neural Networks”. In: *Journal of Computational Physics* 426 (Feb. 1, 2021), p. 109950. ISSN: 0021-9991. DOI: 10.1016/j.jcp.2020.109950.
- [41] Michael Hinze et al., eds. *Optimization with PDE Constraints*. Mathematical Modelling: Theory and Applications 23. New York: Springer, 2009. 270 pp. ISBN: 978-1-4020-8838-4 978-90-481-8003-5.
- [42] S. Hochreiter et al. “Gradient Flow in Recurrent Nets: The Difficulty of Learning LongTerm Dependencies”. In: *A Field Guide to Dynamical Recurrent Networks*. Ed. by J. F. Kolen and S. C. Kremer. Wiley-IEEE Press, 2001, pp. 237–243.
- [43] John David Jackson. *Classical Electrodynamics*. John Wiley & Sons, 1999. ISBN: 978-1-119-77076-3.
- [44] Weinan E Jiequn Han and Qianxiao Li. “Dynamical Systems and Optimal Control Approach to Deep Learning”. In: *Mathematical Aspects of Deep Learning*. Ed. by Gitta Kutyniok and Philipp Grohs. Cambridge: Cambridge University Press, 2022, pp. 422–438. ISBN: 978-1-316-51678-2. DOI: 10.1017/9781009025096.011.

- [45] Pengzhan Jin et al. “SympNets: Intrinsic Structure-Preserving Symplectic Networks for Identifying Hamiltonian Systems”. In: *Neural Networks* 132 (Dec. 1, 2020), pp. 166–179. ISSN: 0893-6080. DOI: 10.1016/j.neunet.2020.08.017.
- [46] F. X. Kärtner et al. “AXSIS: Exploring the Frontiers in Attosecond X-ray Science, Imaging and Spectroscopy”. In: *Nuclear Instruments and Methods in Physics Research Section A: Accelerators, Spectrometers, Detectors and Associated Equipment*. 2nd European Advanced Accelerator Concepts Workshop - EAAC 2015 829 (Sept. 1, 2016), pp. 24–29. ISSN: 0168-9002. DOI: 10.1016/j.nima.2016.02.080.
- [47] Karthik Kashinath, Philip Marcus, et al. “Enforcing Physical Constraints in CNNs through Differentiable PDE Layer”. In: *ICLR 2020 Workshop on Integration of Deep Neural Models and Differential Equations*. 2020.
- [48] Ehsan Kharazmi, Zhongqiang Zhang, and George E.M. Karniadakis. “Hp-VPINNs: Variational Physics-Informed Neural Networks with Domain Decomposition”. In: *Computer Methods in Applied Mechanics and Engineering* 374 (Feb. 2021), p. 113547. ISSN: 00457825. DOI: 10.1016/j.cma.2020.113547.
- [49] Yuehaw Khoo and Lexing Ying. “SwitchNet: A Neural Network Model for Forward and Inverse Scattering Problems”. In: *SIAM Journal on Scientific Computing* 41.5 (2019), A3182–A3201. DOI: 10.1137/18m1222399.
- [50] Diederik P. Kingma and Jimmy Ba. “Adam: A Method for Stochastic Optimization”. In: *3rd International Conference on Learning Representations, ICLR 2015, San Diego, CA, USA, May 7-9, 2015, Conference Track Proceedings*. Ed. by Yoshua Bengio and Yann LeCun. 2015. URL: <http://arxiv.org/abs/1412.6980>.
- [51] Uwe Köcher and Markus Bause. “Variational Space–Time Methods for the Wave Equation”. In: *Journal of Scientific Computing* 61.2 (Nov. 2014), pp. 424–453. ISSN: 0885-7474, 1573-7691. DOI: 10.1007/s10915-014-9831-3.
- [52] Nikola Kovachki, Samuel Lanthaler, and Siddhartha Mishra. “On Universal Approximation and Error Bounds for Fourier Neural Operators”. In: *Journal of Machine Learning Research* 22.290 (2021), pp. 1–76. ISSN: 1533-7928. URL: <http://jmlr.org/papers/v22/21-0806.html>.
- [53] Nikola Kovachki et al. “Neural Operator: Learning Maps Between Function Spaces With Applications to PDEs”. In: *Journal of Machine Learning Research* 24.89 (2023), pp. 1–97. ISSN: 1533-7928. URL: <http://jmlr.org/papers/v24/21-1524.html>.
- [54] I.E. Lagaris, A. Likas, and D.I. Fotiadis. “Artificial Neural Networks for Solving Ordinary and Partial Differential Equations”. In: *IEEE Transactions on Neural Networks* 9.5 (Sept. 1998), pp. 987–1000. ISSN: 1941-0093. DOI: 10.1109/72.712178.
- [55] Ulrich Langer and Olaf Steinbach, eds. *Space-Time Methods: Applications to Partial Differential Equations*. De Gruyter, Sept. 23, 2019. ISBN: 978-3-11-054848-8. DOI: 10.1515/9783110548488.
- [56] Samuel Lanthaler, Siddhartha Mishra, and George E Karniadakis. “Error Estimates for Deep-ONets: A Deep Learning Framework in Infinite Dimensions”. In: *Transactions of Mathematics and Its Applications* 6.1 (Jan. 1, 2022), tnac001. ISSN: 2398-4945. DOI: 10.1093/imatrm/tnac001.
- [57] Zongyi Li et al. “Fourier Neural Operator for Parametric Partial Differential Equations”. In: *International Conference on Learning Representations*. Oct. 2, 2020. URL: <https://openreview.net/forum?id=c8P9NQVtmn0>.

- [58] Xiangru Lian et al. “Can Decentralized Algorithms Outperform Centralized Algorithms? A Case Study for Decentralized Parallel Stochastic Gradient Descent”. In: *Proceedings of the 31st International Conference on Neural Information Processing Systems*. NIPS’17. Red Hook, NY, USA: Curran Associates Inc., Dec. 4, 2017, pp. 5336–5346. ISBN: 978-1-5108-6096-4.
- [59] Dong C. Liu and Jorge Nocedal. “On the Limited Memory BFGS Method for Large Scale Optimization”. In: *Mathematical Programming* 45.1 (Aug. 1, 1989), pp. 503–528. ISSN: 1436-4646. DOI: 10.1007/BF01589116.
- [60] Guan-Horng Liu and Evangelos A. Theodorou. *Deep Learning Theory Review: An Optimal Control and Dynamical Systems Perspective*. Sept. 28, 2019. DOI: 10.48550/arXiv.1908.10920. arXiv: 1908.10920 [cs, eess, stat]. preprint.
- [61] Lu Lu, Pengzhan Jin, and George Em Karniadakis. “DeepONet: Learning Nonlinear Operators for Identifying Differential Equations Based on the Universal Approximation Theorem of Operators”. 2019. arXiv: 1910.03193.
- [62] Lu Lu, Pengzhan Jin, and George Em Karniadakis. “DeepONet: Learning Nonlinear Operators for Identifying Differential Equations Based on the Universal Approximation Theorem of Operators”. In: *Nature Machine Intelligence* 3.3 (Mar. 2021), pp. 218–229. ISSN: 2522-5839. DOI: 10.1038/s42256-021-00302-5. arXiv: 1910.03193.
- [63] Lu Lu et al. “DeepXDE: A Deep Learning Library for Solving Differential Equations”. In: *SIAM Review* 63.1 (Jan. 2021), pp. 208–228. ISSN: 0036-1445. DOI: 10.1137/19M1274067.
- [64] Andrea Manzoni, Alfio Quarteroni, and Sandro Salsa. *Optimal Control of Partial Differential Equations: Analysis, Approximation, and Applications*. Vol. 207. Applied Mathematical Sciences. Cham: Springer International Publishing, 2021. ISBN: 978-3-030-77225-3 978-3-030-77226-0. DOI: 10.1007/978-3-030-77226-0.
- [65] Nils Margenberg, Franz Kaertner, and Markus Bause. “Accurate Simulation of THz Generation with Finite-Element Time Domain Methods”. In: *Optics Express* (Mar. 27, 2023). ISSN: 1094-4087. DOI: 10.1364/OE.480793.
- [66] M. Mattheakis et al. “Physical Symmetries Embedded in Neural Networks”. Apr. 2019. arXiv: 1904.08991. URL: <http://arxiv.org/abs/1904.08991>.
- [67] G Matthies and F Schieweck. “Higher Order Variational Time Discretizations for Nonlinear Systems of Ordinary Differential Equations”. In: *Preprint* (2011), p. 30.
- [68] Roberto Molinaro et al. *Neural Inverse Operators for Solving PDE Inverse Problems*. Jan. 26, 2023. arXiv: 2301.11167 [math-ph]. URL: <http://arxiv.org/abs/2301.11167>. preprint.
- [69] Nicholas H Nelsen and Andrew M Stuart. “The Random Feature Model for Input-Output Maps between Banach Spaces”. In: *SIAM Journal on Scientific Computing* 43.5 (2021), A3212–A3243. DOI: 10.1137/20m133957x.
- [70] Geoffrey New. *Introduction to Nonlinear Optics*. Cambridge: Cambridge University Press, 2011. ISBN: 978-0-521-87701-5. DOI: 10.1017/CB09780511975851.
- [71] Thomas O’Leary-Roseberry et al. “Derivative-Informed Projected Neural Networks for High-Dimensional Parametric Maps Governed by PDEs”. In: *Computer Methods in Applied Mechanics and Engineering* 388 (Jan. 1, 2022), p. 114199. ISSN: 0045-7825. DOI: 10.1016/j.cma.2021.114199.

- [72] H. T. Olgun et al. “Highly Efficient Generation of Narrowband Terahertz Radiation Driven by a Two-Spectral-Line Laser in PPLN”. In: *Optics Letters* 47.10 (May 15, 2022), pp. 2374–2377. ISSN: 1539-4794. DOI: 10.1364/OL.448457.
- [73] Joost A.A. Opschoor, Christoph Schwab, and Jakob Zech. “Deep Learning in High Dimension: ReLU Network Expression Rates for Bayesian PDE Inversion”. In: *SAM Research Report 2020–47* (2020).
- [74] Shaowu Pan and Karthik Duraisamy. “Physics-Informed Probabilistic Learning of Linear Embeddings of Nonlinear Dynamics with Guaranteed Stability”. In: *SIAM Journal on Applied Dynamical Systems* 19.1 (2020), pp. 480–509. DOI: 10.1137/19m1267246.
- [75] Adam Paszke et al. “PyTorch: An Imperative Style, High-Performance Deep Learning Library”. In: *Advances in Neural Information Processing Systems* 32. Ed. by H. Wallach et al. Curran Associates, Inc., 2019, pp. 8024–8035. URL: <http://papers.neurips.cc/paper/9015-pytorch-an-imperative-style-high-performance-deep-learning-library.pdf>.
- [76] Ilaria Perugia et al. “Tent Pitching and Trefftz-DG Method for the Acoustic Wave Equation”. In: *Computers & Mathematics with Applications* 79.10 (May 15, 2020), pp. 2987–3000. ISSN: 0898-1221. DOI: 10.1016/j.camwa.2020.01.006.
- [77] Christopher Rackauckas et al. “Universal Differential Equations for Scientific Machine Learning”. Aug. 6, 2020. arXiv: 2001.04385 [cs, math, q-bio, stat]. URL: <http://arxiv.org/abs/2001.04385>.
- [78] Maziar Raissi, Paris Perdikaris, and George E Karniadakis. “Physics-Informed Neural Networks: A Deep Learning Framework for Solving Forward and Inverse Problems Involving Nonlinear Partial Differential Equations”. In: *Journal of Computational Physics* 378 (2019), pp. 686–707. DOI: 10.1016/j.jcp.2018.10.045.
- [79] Lars Ruthotto et al. “A Machine Learning Framework for Solving High-Dimensional Mean Field Game and Mean Field Control Problems”. In: *Proceedings of the National Academy of Sciences* 117.17 (Apr. 28, 2020), pp. 9183–9193. ISSN: 0027-8424, 1091-6490. DOI: 10.1073/pnas.1922204117.
- [80] Christoph Schwab and Jakob Zech. “Deep Learning in High Dimension: Neural Network Expression Rates for Generalized Polynomial Chaos Expansions in UQ”. In: *Analysis and Applications* 17.01 (2019), pp. 19–55. DOI: 10.1142/s0219530518500203.
- [81] Jacob H. Seidman et al. “Robust Deep Learning as Optimal Control: Insights and Convergence Guarantees”. In: *Proceedings of the 2nd Conference on Learning for Dynamics and Control*. Learning for Dynamics and Control. PMLR, July 31, 2020, pp. 884–893. URL: <https://proceedings.mlr.press/v120/seidman20a.html>.
- [82] Justin Sirignano and Konstantinos Spiliopoulos. “DGM: A Deep Learning Algorithm for Solving Partial Differential Equations”. In: *Journal of computational physics* 375 (2018), pp. 1339–1364. DOI: 10.1016/j.jcp.2018.08.029.
- [83] Olaf Steinbach and Marco Zank. “Coercive Space-Time Finite Element Methods for Initial Boundary Value Problems”. In: *ETNA - Electronic Transactions on Numerical Analysis* 52 (2020), pp. 154–194. ISSN: 1068-9613, 1068-9613. DOI: 10.1553/etna_vol52s154.

- [84] E Weinan, Jiequn Han, and Jihao Long. “Empowering Optimal Control with Machine Learning: A Perspective from Model Predictive Control”. In: *IFAC-PapersOnLine*. 25th International Symposium on Mathematical Theory of Networks and Systems MTNS 2022 55.30 (Jan. 1, 2022), pp. 121–126. ISSN: 2405-8963. DOI: 10.1016/j.ifacol.2022.11.039.

A. Derivation of the fully discrete system

Here, we elaborate on the derivation of the fully discrete problems carried out in Section 2. We discretize Problem 2.2 and particularly describe the steps necessary to obtain the fully discrete, global in time Problem 3.1 with the equation (3.5) from (2.2). We derive the local fully discrete problem, which, as discussed in Section 3, leads to the global fully discrete problem 3.1. Finally, we describe the solution of the local, fully discrete problems by a Newton linearization in combination with the solvers for the arising linear systems of equations.

Following [2], we define $\{\phi_j\}_{j=1}^J \subset \mathcal{V}_h$ as a (global) nodal Lagrangian basis of \mathcal{V}_h and the Hermite-type basis of $\mathbb{P}_3(\hat{I}; \mathbb{R})$, where $\hat{I} := [0, 1]$:

$$\hat{\xi}_0(t) = 1 - 3t^2 + 2t^3 \quad \hat{\xi}_1(t) = t - 2t^2 + t^3 \quad \hat{\xi}_2(t) = 3t^2 - 2t^3 \quad \hat{\xi}_3(t) = -t^2 + t^3.$$

With the affine transformation

$$\mathbf{T}_n : \begin{cases} \hat{I} & \rightarrow I_n \\ \hat{t} & \mapsto t_{n-1} + (t_n - t_{n-1})\hat{t} \end{cases}$$

the basis $\{\xi_i\}_{i=0}^3$ on I_n is given by the composition of $\hat{\xi}_l \circ \mathbf{T}_n^{-1} =: \xi_l$ for $l = 0, \dots, 3$. Functions $\mathbf{w}_{\tau,h} \in \mathbb{P}_3(I_n; \mathcal{V}_h)$ are thus represented as

$$\mathbf{w}_{\tau,h}(x, t) = \sum_{i=0}^3 \mathbf{w}_{n,i}(x) \xi_i(t) = \sum_{i=0}^3 \sum_{j=1}^J \mathbf{w}_{n,i,j} \phi_j(x) \xi_i(t), \quad \text{for } (x, t) \in \Omega \times \bar{I}_n. \quad (\text{A.1})$$

We adopt the representation (A.1) for the variables \mathbf{u} , \mathbf{p} , \mathbf{e} , \mathbf{a} and choose test functions from $\mathbb{P}_0(I_n; \mathcal{V}_h)$. A test basis of $\mathbb{P}_0(I_n, \mathcal{V}_h)$ is then given by

$$\mathcal{B} = \{ \phi_i \mathbf{1}_{I_n} \}_{i=1}^J. \quad (\text{A.2})$$

Let $\mathbf{A}_h^0 : V_0 \rightarrow \mathcal{V}_{h,0}$ be the discrete operator that is defined by

$$\langle \mathbf{A}_h \mathbf{e}_h, \phi_h \rangle = \langle \nabla \mathbf{e}_h, \nabla \phi_h \rangle \quad \forall \phi_h \in \mathcal{V}_{h,0}. \quad (\text{A.3})$$

We define $V_{g_h} := \{ \mathbf{v} \in V \mid \mathbf{v} = g_h \text{ on } \Gamma_D \}$ and $\mathbf{A}_h : V_{g_h} \rightarrow \mathcal{V}_h$, $\mathbf{w} \mapsto \mathbf{A}_h \mathbf{w}$. By the definition of V_{g_h} , \mathbf{w} admits the representation $\mathbf{w} = \mathbf{w}^0 + g_h$ and we define \mathbf{A}_h by

$$\mathbf{A}_h \mathbf{w} = \mathbf{A}_h^0 \mathbf{w}^0 + g_h. \quad (\text{A.4})$$

For $\mathbf{w} \in \{\mathbf{u}, \mathbf{p}, \mathbf{a}, \mathbf{e}\}$, we denote the right and left-hand limit by

$$\partial_t^i \mathbf{w}_{n,h}^- = \lim_{t \nearrow t_n} \partial_t^i \mathbf{w}_{\tau,h}(t), \quad \partial_t^i \mathbf{w}_{n,h}^+ = \lim_{t \searrow t_n} \partial_t^i \mathbf{w}_{\tau,h}(t), \quad \text{for } i \in \{0, 1\}. \quad (\text{A.5})$$

Recall the fully discrete, global formulation of the GCC¹(3) method Problem 3.1. Now consider the local problem on the interval I_n where the trajectories $\mathbf{e}_{\tau,h}(t)$, $\mathbf{a}_{\tau,h}(t)$, $\mathbf{p}_{\tau,h}(t)$, and $\mathbf{u}_{\tau,h}(t)$ have already been computed for all $t \in [0, t_{n-1}]$ with initial conditions $\mathbf{e}_{\tau,h}(0) = \mathbf{e}_{0,h}$, $\mathbf{a}_{\tau,h}(0) = \mathbf{a}_{0,h}$, $\mathbf{p}_{\tau,h}(0) = \mathbf{p}_{0,h}$ and $\mathbf{u}_{\tau,h}(0) = \mathbf{u}_{0,h}$. Then we solve the following local problem:

Problem A.1: Local, fully discrete, GCC¹(3) method for (2.4)

Given $(\mathbf{e}_{\tau,h}(t_{n-1}), \mathbf{a}_{\tau,h}(t_{n-1}), \mathbf{p}_{\tau,h}(t_{n-1}), \mathbf{u}_{\tau,h}(t_{n-1})) \in \mathcal{V}_h^4$, find $(\mathbf{e}_{\tau,h}, \mathbf{a}_{\tau,h}, \mathbf{p}_{\tau,h}, \mathbf{u}_{\tau,h}) \in (\mathbb{P}_3(I_n; \mathcal{V}_h))^4$ such that $e_{\tau,h} = g_{\tau,h}^e$ on $\bar{I}_n \times \Gamma_D$ and

$$\mathbf{w}_{n-1,h}^+ = \mathbf{w}_{n-1,h}^- \quad \forall \mathbf{w} \in \{\mathbf{e}, \mathbf{a}, \mathbf{p}, \mathbf{u}\}, \quad (\text{A.6a})$$

$$\partial_t \mathbf{w}_{n-1,h}^+ = \partial_t \mathbf{w}_{n-1,h}^- \quad \forall \mathbf{w} \in \{\mathbf{e}, \mathbf{a}, \mathbf{p}, \mathbf{u}\}, \quad (\text{A.6b})$$

$$-\mathbf{u}_{n,h}^- + \partial_t \mathbf{p}_{n,h}^- + \Gamma_0 \mathbf{p}_{n,h}^- = 0, \quad (\text{A.6c})$$

$$v_t^2 \mathbf{p}_{n,h}^- - v_t^2 \varepsilon_\Delta \mathbf{e}_{n,h}^- + \partial_t \mathbf{u}_{n,h}^- = 0, \quad (\text{A.6d})$$

$$-\Gamma_0 \mathbf{p}_{n,h}^- + \chi^{(2)} \partial_t (|\mathbf{e}_{n,h}^-| \mathbf{e}_{n,h}^-) + \varepsilon_\omega \partial_t \mathbf{e}_{n,h}^- - \mathbf{a}_{n,h}^- = 0, \quad (\text{A.6e})$$

$$v_t^2 \varepsilon_\Delta \mathbf{e}_{n,h}^- + \mathbf{A}_h \mathbf{e}_{n,h}^- - v_t^2 \mathbf{p}_{n,h}^- + \partial_t \mathbf{a}_{n,h}^- = \mathbf{f}_{n,h}^-, \quad (\text{A.6f})$$

and for all $(\phi_{\tau,h}^0, \phi_{\tau,h}^1, \phi_{\tau,h}^2, \phi_{\tau,h}^3) \in (\mathbb{P}_0(I_n; \mathcal{V}_{h,0}))^4$,

$$\int_{t_{n-1}}^{t_n} \langle \partial_t \mathbf{p}_{\tau,h}^n, \phi_{\tau,h}^0 \rangle + \Gamma_0 \langle \mathbf{p}_{\tau,h}^n, \phi_{\tau,h}^0 \rangle - \langle \mathbf{u}_{\tau,h}^n, \phi_{\tau,h}^0 \rangle dt = 0, \quad (\text{A.7a})$$

$$\int_{t_{n-1}}^{t_n} v_t^2 \langle \mathbf{p}_{\tau,h}^n, \phi_{\tau,h}^1 \rangle - \varepsilon_\Delta v_t^2 \langle \mathbf{e}_{\tau,h}^n, \phi_{\tau,h}^1 \rangle + \langle \partial_t \mathbf{u}_{\tau,h}^n, \phi_{\tau,h}^1 \rangle dt = 0, \quad (\text{A.7b})$$

$$\int_{t_{n-1}}^{t_n} \varepsilon_\omega \langle \partial_t \mathbf{e}_{\tau,h}^n, \phi_{\tau,h}^2 \rangle - \Gamma_0 \langle \mathbf{p}_{\tau,h}^n, \phi_{\tau,h}^2 \rangle + \chi^{(2)} \langle \partial_t (|\mathbf{e}_{\tau,h}^n| \mathbf{e}_{\tau,h}^n), \phi_{\tau,h}^2 \rangle - \langle \mathbf{a}_{\tau,h}^n, \phi_{\tau,h}^2 \rangle dt = 0, \quad (\text{A.7c})$$

$$\int_{t_{n-1}}^{t_n} \langle \nabla \mathbf{e}_{\tau,h}^n, \nabla \phi_{\tau,h}^3 \rangle + (\varepsilon_\Omega - \varepsilon_\omega) v_t^2 \langle \mathbf{e}_{\tau,h}^n, \phi_{\tau,h}^3 \rangle - v_t^2 \langle \mathbf{p}_{\tau,h}^n, \phi_{\tau,h}^3 \rangle + \langle \partial_t \mathbf{a}_{\tau,h}^n, \phi_{\tau,h}^3 \rangle dt = \int_{t_{n-1}}^{t_n} \langle \mathbf{f}_{\tau,h}, \phi_{\tau,h}^3 \rangle dt. \quad (\text{A.7d})$$

We comment on the local fully discrete problem A.1:

- Note that we evaluate the time integrals on the right-hand side of (A.7d) and the boundary conditions $g_{\tau,h}^e \in C^1(\bar{I}; \mathcal{V}_h)$ (cf. Assumption 3.1) using the Hermite-type interpolation operator $I_\tau|_{I_n}$ on I_n , defined by

$$I_\tau|_{I_n} g(t) = \hat{\xi}_0(0) g|_{I_n}(t_{n-1}) + \tau_n \hat{\xi}_1(0) \partial_t g|_{I_n}(t_{n-1}) + \hat{\xi}_2(1) g|_{I_n}(t_{n-1}) + \tau_n \hat{\xi}_3(1) \partial_t g|_{I_n}(t_{n-1}). \quad (\text{A.8})$$

- The collocation conditions (A.6b) need to be defined at the initial time t_0 . From the initial conditions we can get the collocation conditions (A.6b) at the initial timepoints by setting

$$\partial_t \mathbf{u}_{\tau,h}(t_0^-) = v_t^2 \varepsilon_\Delta \mathbf{e}_{0,h} - v_t^2 \mathbf{p}_{0,h}, \quad (\text{A.9a})$$

$$\partial_t \mathbf{p}_{\tau,h}(t_0^-) = \mathbf{u}_{0,h} - \Gamma_0 \mathbf{p}_{0,h}, \quad (\text{A.9b})$$

$$\partial_t \mathbf{a}_{\tau,h}(t_0^-) = v_t^2 \mathbf{p}_{0,h} - \mathbf{A}_h \mathbf{e}_{0,h} - v_t^2 \varepsilon_\Delta \mathbf{e}_{0,h}, \quad (\text{A.9c})$$

$$\partial_t \mathbf{e}_{\tau,h}(t_0^-) = \varepsilon_\Delta^{-1} (\mathbf{a}_{0,h} - \chi^{(2)} \partial_t (|\mathbf{e}_{0,h}| \mathbf{e}_{0,h}) + \Gamma_0 \mathbf{p}_{0,h}). \quad (\text{A.9d})$$

- Consider a time interval I_l , $l = 2, \dots, N$. We previously solved the Problem A.1 on I_{l-1} . At t_{l-1} the

collocation conditions (A.6c)–(A.6f) are fulfilled. For (A.6e), we see that

$$\begin{aligned} & -\Gamma_0 \mathbf{p}_{l,h}^+ + \chi^{(2)} \partial_t (|\mathbf{e}_{l,h}^+| \mathbf{e}_{l,h}^+) + \varepsilon_\omega \partial_t \mathbf{e}_{l,h}^+ - \mathbf{a}_{l,h}^+ - (-\Gamma_0 \mathbf{p}_{l,h}^- + \chi^{(2)} \partial_t (|\mathbf{e}_{l,h}^-| \mathbf{e}_{l,h}^-) + \varepsilon_\omega \partial_t \mathbf{e}_{l,h}^- - \mathbf{a}_{l,h}^-) \\ & = \chi^{(2)} |\mathbf{e}_{l,h}^+| (\partial_t \mathbf{e}_{l,h}^+) - \chi^{(2)} |\mathbf{e}_{l,h}^-| (\partial_t \mathbf{e}_{l,h}^-) + \chi^{(2)} \mathbf{e}_{l,h}^+ (\partial_t |\mathbf{e}_{l,h}^+|) - \chi^{(2)} \mathbf{e}_{l,h}^- (\partial_t |\mathbf{e}_{l,h}^-|) = 0, \end{aligned}$$

by using (A.6a) and (A.6b) componentwise. The remaining conditions (A.6c)–(A.6f) follow immediately. Therefore, upon solving Problem A.1 on I_l the equations

$$-\mathbf{u}_{l,h} + \partial_t \mathbf{p}_{l,h} + \Gamma_0 \mathbf{p}_{l,h} = 0, \quad (\text{A.10a})$$

$$v_t^2 \mathbf{p}_{l,h} - v_t^2 \varepsilon_\Delta \mathbf{e}_{l,h} + \partial_t \mathbf{u}_{l,h} = 0, \quad (\text{A.10b})$$

$$-\Gamma_0 \mathbf{p}_{l,h} + \chi^{(2)} \partial_t (|\mathbf{e}_{l,h}| \mathbf{e}_{l,h}) + \varepsilon_\omega \partial_t \mathbf{e}_{l,h} - \mathbf{a}_{l,h} = 0, \quad (\text{A.10c})$$

$$v_t^2 \varepsilon_\Delta \mathbf{e}_{l,h} + \mathbf{A}_h \mathbf{e}_{l,h} - v_t^2 \mathbf{p}_{l,h} + \partial_t \mathbf{a}_{l,h} = \mathbf{f}_{l,h}, \quad (\text{A.10d})$$

hold. This justifies the notion of a collocation method and shows that, from the initial timepoint on, global C^1 -regularity is achieved by enforcing it from time step to time step.

We put the equations of the proposed GCC¹(3) approach in their algebraic forms. In the variational equations (A.7), we use the representation (A.1) for each component of $(\mathbf{e}_{\tau,h}, \mathbf{a}_{\tau,h}, \mathbf{p}_{\tau,h}, \mathbf{u}_{\tau,h}) \in (\mathbb{P}_3(I_n; \mathcal{V}_h))^4$ and choose the piecewise constant test functions. We interpolate the right-hand sides in (A.7) by applying the Hermite interpolation and evaluate the arising time integrals analytically. The collocation conditions (A.6) can be recovered in their algebraic forms by using the fact that the Hermite type polynomials and their first derivatives vanish at the locations $x = 0$ and $x = 1$, with the exceptions $\xi_0(0) = 1$, $\partial_t \xi_1(0) = 1$, $\xi_2(1) = 1$, $\partial_t \xi_3(1) = 1$.

Given the local Problem A.1 on the interval I_n and (A.1), we introduce the abbreviations $\mathbf{w}_{h,i} = \mathbf{w}_{n,i}(x) \in \mathcal{V}_h$ and $\mathbf{w}_i = (\mathbf{w}_{n,i,0}, \dots, \mathbf{w}_{n,i,J})^\top \in \mathbb{R}^J$ for $\mathbf{w} \in \{\mathbf{q}, \mathbf{r}, \mathbf{u}, \mathbf{p}, \mathbf{e}, \mathbf{a}\}$. Further we define

$$\mathbf{v}_{h,r} = (\mathbf{e}_{0,h} \ \mathbf{e}_{1,h} \ \mathbf{a}_{0,h} \ \mathbf{a}_{1,h})^\top \text{ and } \mathbf{v}_{h,l} = (\mathbf{e}_{2,h} \ \mathbf{e}_{3,h} \ \mathbf{a}_{2,h} \ \mathbf{a}_{3,h})^\top. \quad (\text{A.11a})$$

Then we condense the system of equations such that we solve for $\mathbf{e}_{2,h}, \mathbf{e}_{3,h}, \mathbf{a}_{2,h}, \mathbf{a}_{3,h}$. Solving for the unknowns $\mathbf{p}_{2,h}, \mathbf{p}_{3,h}, \mathbf{u}_{2,h}, \mathbf{u}_{3,h}$ reduces to simple vector identities in their algebraic form. We write the nonlinear system of equations in variational form for each subinterval I_n as

$$\mathcal{A}_{h,n}(\mathbf{v}_{h,l})(\Phi) = \mathbf{F}_{h,n}(\Phi; \mathbf{v}_{h,r}) \quad \forall \Phi \in \mathcal{V}_h^4, \quad (\text{A.12})$$

where $\mathcal{A}_{h,n} : \mathcal{V}_h^4 \times \mathcal{V}_h^4 \rightarrow \mathbb{R}$ is a semilinear form and $\mathbf{F}_{h,n}(\Phi; \mathbf{v}_r)$ the right-hand side. Then $\mathcal{A}_{h,n}$ and the functional $\mathbf{F}_{h,n}$ in (A.12) are defined through

$$\mathcal{A}_{h,n}(\mathbf{v}_{h,l})(\phi) = \mathcal{A}_{h,n}^1(\mathbf{v}_{h,l})(\phi) + \mathcal{A}_{h,n}^2(\mathbf{v}_{h,l})(\phi) + \mathcal{A}_{h,n}^3(\mathbf{v}_{h,l})(\phi) + \mathcal{A}_{h,n}^4(\mathbf{v}_{h,l})(\phi), \quad (\text{A.13a})$$

with the components $\mathcal{A}_{h,n}^i$, $i = 1, \dots, 3$. The components represent the block structure of the system

of equations in algebraic form. The components given as

$$\begin{aligned} \mathcal{A}_{h,n}^1(\mathbf{v}_{h,l})(\boldsymbol{\phi}) &= -\frac{\Gamma_0}{v_t^2} \langle \nabla \mathbf{e}_{h,2}, \nabla \boldsymbol{\phi} \rangle - \varepsilon_\Delta \Gamma_0 \langle \mathbf{e}_{h,2}, \boldsymbol{\phi} \rangle - \langle \mathbf{a}_{h,2}, \boldsymbol{\phi} \rangle \\ &\quad + \chi^{(2)} \langle |\mathbf{e}_{h,3}| \mathbf{e}_{h,3}, \boldsymbol{\phi} \rangle + \frac{\varepsilon_\omega}{k} \langle \mathbf{e}_{h,3}, \boldsymbol{\phi} \rangle - \frac{\Gamma_0}{kv_t^2} \langle \mathbf{a}_{h,3}, \boldsymbol{\phi} \rangle, \end{aligned} \quad (\text{A.13b})$$

$$\begin{aligned} \mathcal{A}_{h,n}^2(\mathbf{v}_{h,l})(\boldsymbol{\phi}) &= \varepsilon_\Delta \langle \mathbf{e}_{h,2}, \boldsymbol{\phi} \rangle - \frac{k^2 v_t^2 - 12}{12v_t^2} \langle \nabla \mathbf{e}_{h,2}, \nabla \boldsymbol{\phi} \rangle + \frac{k\Gamma_0 + 6}{kv_t^2} \langle \mathbf{a}_{h,2}, \boldsymbol{\phi} \rangle \\ &\quad - \frac{k\Gamma_0 + 6}{12v_t^2} \langle \nabla \mathbf{e}_{h,3}, \nabla \boldsymbol{\phi} \rangle - \frac{\varepsilon_\Delta (k\Gamma_0 + 6)}{12} \langle \mathbf{e}_{h,3}, \boldsymbol{\phi} \rangle - \frac{k^2 v_t^2 + 6k\Gamma_0 + 24}{12kv_t^2} \langle \mathbf{a}_{h,3}, \boldsymbol{\phi} \rangle, \end{aligned} \quad (\text{A.13c})$$

$$\begin{aligned} \mathcal{A}_{h,n}^3(\mathbf{v}_{h,l})(\boldsymbol{\phi}) &= \frac{kv_t^2 + 2\Gamma_0}{2v_t^2} \langle \nabla \mathbf{e}_{h,2}, \nabla \boldsymbol{\phi} \rangle + \varepsilon_\Delta \Gamma_0 \langle \mathbf{e}_{h,2}, \boldsymbol{\phi} \rangle + \frac{k^2 v_t^2 - 12}{k^2 v_t^2} \langle \mathbf{a}_{h,2}, \boldsymbol{\phi} \rangle \\ &\quad + \frac{\varepsilon_\Delta}{k} \langle \mathbf{e}_{h,3}, \boldsymbol{\phi} \rangle - \frac{k^2 v_t^2 - 12}{12kv_t^2} \langle \nabla \mathbf{e}_{h,3}, \nabla \boldsymbol{\phi} \rangle + \frac{k\Gamma_0 + 6}{k^2 v_t^2} \langle \mathbf{a}_{h,3}, \boldsymbol{\phi} \rangle, \end{aligned} \quad (\text{A.13d})$$

$$\begin{aligned} \mathcal{A}_{h,n}^4(\mathbf{v}_{h,l})(\boldsymbol{\phi}) &= \frac{2\varepsilon_\omega - k\varepsilon_\Delta \Gamma_0}{2} \langle \mathbf{e}_{h,2}, \boldsymbol{\phi} \rangle - \frac{k\Gamma_0}{2v_t^2} \langle \nabla \mathbf{e}_{h,2}, \nabla \boldsymbol{\phi} \rangle - \frac{kv_t^2 + 2\Gamma_0}{2v_t^2} \langle \mathbf{a}_{h,2}, \boldsymbol{\phi} \rangle \\ &\quad + \chi^{(2)} \langle |\mathbf{e}_2| \mathbf{e}_2, \boldsymbol{\phi} \rangle + \frac{k\Gamma_0}{12v_t^2} \langle \nabla \mathbf{e}_{h,3}, \nabla \boldsymbol{\phi} \rangle + \frac{k\varepsilon_\Delta \Gamma_0}{12} \langle \mathbf{e}_{h,3}, \boldsymbol{\phi} \rangle + \frac{k}{12} \langle \mathbf{a}_{h,3}, \boldsymbol{\phi} \rangle, \end{aligned} \quad (\text{A.13e})$$

and with an analogous splitting of $\mathbf{F}_{h,n}$

$$\mathbf{F}_{h,n}^1(\boldsymbol{\Phi}; \mathbf{v}_{h,r}) = 0, \quad (\text{A.13f})$$

$$\begin{aligned} \mathbf{F}_{h,n}^2(\boldsymbol{\Phi}; \mathbf{v}_{h,r}) &= -\frac{k\Gamma_0 + 6}{12v_t^2} (\langle \nabla \mathbf{e}_{h,1}, \nabla \boldsymbol{\phi} \rangle + \langle \nabla \mathbf{e}_{h,0}, \nabla \boldsymbol{\phi} \rangle) - \frac{\varepsilon_\Delta (k\Gamma_0 + 6)}{12} (\langle \mathbf{e}_{h,1}, \boldsymbol{\phi} \rangle + \langle \mathbf{e}_{h,0}, \boldsymbol{\phi} \rangle) \\ &\quad + \frac{k\Gamma_0 + 6}{kv_t^2} \langle \mathbf{a}_{h,0}, \boldsymbol{\phi} \rangle + \frac{k}{12} \langle \mathbf{u}_{h,1}, \boldsymbol{\phi} \rangle + \frac{k}{2} \langle \mathbf{u}_{h,0}, \boldsymbol{\phi} \rangle + \frac{1}{2} \langle \mathbf{p}_{h,1}, \boldsymbol{\phi} \rangle + \langle 4\mathbf{p}_{h,0}, \boldsymbol{\phi} \rangle, \end{aligned} \quad (\text{A.13g})$$

$$\begin{aligned} \mathbf{F}_{h,n}^3(\boldsymbol{\Phi}; \mathbf{v}_{h,r}) &= \frac{\varepsilon_\Delta}{k} \langle \mathbf{e}_{h,1}, \boldsymbol{\phi} \rangle - \frac{k^2 v_t^2 - 12}{12kv_t^2} \langle \nabla \mathbf{e}_{h,1}, \nabla \boldsymbol{\phi} \rangle + \frac{6\varepsilon_\Delta}{k} \langle \mathbf{e}_{h,0}, \boldsymbol{\phi} \rangle - \frac{k^2 v_t^2 - 12}{2kv_t^2} \langle \nabla \mathbf{e}_{h,0}, \nabla \boldsymbol{\phi} \rangle \\ &\quad + \frac{k^2 v_t^2 - 12}{k^2 v_t^2} \langle \mathbf{a}_{h,0}, \boldsymbol{\phi} \rangle + \langle \mathbf{u}_{h,0}, \boldsymbol{\phi} \rangle - \frac{1}{k} \langle \mathbf{p}_{h,1}, \boldsymbol{\phi} \rangle - \frac{6}{k} \langle \mathbf{p}_{h,0}, \boldsymbol{\phi} \rangle, \end{aligned} \quad (\text{A.13h})$$

$$\begin{aligned} \mathbf{F}_{h,n}^4(\boldsymbol{\Phi}; \mathbf{v}_{h,r}) &= \frac{k\varepsilon_\Delta \Gamma_0 + 2\varepsilon_\omega}{2} \langle \mathbf{e}_{h,0}, \boldsymbol{\phi} \rangle + \frac{k\Gamma_0}{2v_t^2} \langle \nabla \mathbf{e}_{h,0}, \nabla \boldsymbol{\phi} \rangle + \frac{k\Gamma_0}{12v_t^2} \langle \nabla \mathbf{e}_{h,1}, \nabla \boldsymbol{\phi} \rangle + \frac{k\varepsilon_\Delta \Gamma_0}{12} \langle \mathbf{e}_{h,1}, \boldsymbol{\phi} \rangle \\ &\quad + \chi^{(2)} \langle |\mathbf{e}_0| \mathbf{e}_0, \boldsymbol{\phi} \rangle + \frac{kv_t^2 - 2\Gamma_0}{2v_t^2} \langle \mathbf{a}_{h,0}, \boldsymbol{\phi} \rangle + \frac{k}{12} \langle \mathbf{a}_{h,1}, \boldsymbol{\phi} \rangle. \end{aligned} \quad (\text{A.13i})$$

As a result of the condensation we further get update equations for the variables \mathbf{p}_2 , \mathbf{u}_2 , \mathbf{p}_3 , \mathbf{u}_3

$$\mathbf{u}_2 = -\frac{6\Gamma_0}{kv_t^2} \mathbf{u}_0 - \frac{6}{k} \mathbf{p}_0 + \frac{\Gamma_0}{kv_t^2} \mathbf{u}_1 - \frac{1}{k} \mathbf{p}_1 + \frac{\varepsilon_\Delta}{k} (6\mathbf{e}_0 + \mathbf{e}_1 - \Gamma_0 k \mathbf{e}_2 - \mathbf{e}_3), \quad (\text{A.14a})$$

$$\mathbf{p}_2 = \frac{\Gamma_0}{v_t^2} \mathbf{u}_2 + \frac{6}{kv_t^2} \mathbf{u}_0 - \frac{6(k\Gamma_0 - 2)}{k^2 v_t^2} \mathbf{p}_0 + \frac{1}{kv_t^2} \mathbf{u}_1 - \frac{\Gamma_0}{kv_t^2} \mathbf{p}_1 - \varepsilon_\Delta \mathbf{e}_2, \quad (\text{A.14b})$$

$$\mathbf{u}_3 = kv_t^2 \mathbf{p}_2 - k\varepsilon_\Delta v_t^2 \mathbf{e}_2, \quad (\text{A.14c})$$

$$\mathbf{p}_3 = k\Gamma_0 \mathbf{p}_2 - k\mathbf{u}_2. \quad (\text{A.14d})$$

The common approach of handling the nonlinear problem is a linearization by means of Newton's method. Let

$$\mathbf{x} \in \mathcal{V}_h : \mathcal{A}_{h,n}(\mathbf{x})(\boldsymbol{\phi}) = \mathbf{F}(\boldsymbol{\phi}) \quad \forall \boldsymbol{\phi} \in \mathcal{V}_h \quad (\text{A.15})$$

be the variational equation related to (A.12). Recall that $\mathcal{A}_{h,n}(\bullet)(\bullet)$ of (A.13a) is a semi-linear form which is linear in the second argument. We assume that it is sufficiently differentiable by means of the Gateaux derivative $\mathcal{A}'_{h,n}(\mathbf{x})(\delta\mathbf{x}, \boldsymbol{\phi}) := \frac{d}{ds}\mathcal{A}_{h,n}(\mathbf{x} + \varepsilon\delta\mathbf{x})(\boldsymbol{\phi})|_{\varepsilon=0}$. $\mathcal{A}'_{h,n}$ denotes the derivative of $\mathcal{A}_{h,n}$ at $\mathbf{x} \in \mathcal{V}_h$ in direction $\delta\mathbf{x} \in \mathcal{V}_h$. The Newton iteration for solving (A.15) with an initial guess $\mathbf{x}_0 \in \mathcal{V}_h$ iterates for $m = 0, \dots$

$$\begin{aligned} \delta\mathbf{x}_m : \mathcal{A}'_{h,n}(\mathbf{x}_{m-1})(\delta\mathbf{x}_m, \boldsymbol{\phi}) &= F(\boldsymbol{\phi}) - \mathcal{A}_{h,n}(\mathbf{x}_{m-1})(\boldsymbol{\phi}) \quad \forall \boldsymbol{\phi} \in \mathcal{V}_h, \\ \mathbf{x}_m &:= \mathbf{x}_{m-1} + \delta\mathbf{x}_m. \end{aligned} \quad (\text{A.16})$$

Next we apply the Newton scheme to the system (A.12). The Gateaux derivative $\mathcal{A}'_{h,n}(\mathbf{x})(\delta\mathbf{x}, \boldsymbol{\phi})$ is

$$\begin{aligned} \mathcal{A}'_{h,n}{}^1(\mathbf{x})(\delta\mathbf{x}, \boldsymbol{\phi}) &= -\frac{\Gamma_0}{v_t^2} \langle \nabla \delta \mathbf{e}_{h,2}, \nabla \boldsymbol{\phi} \rangle - \varepsilon_\Delta \Gamma_0 \langle \delta \mathbf{e}_{h,2}, \boldsymbol{\phi} \rangle - \langle \delta \mathbf{a}_{h,2}, \boldsymbol{\phi} \rangle \\ &\quad + \chi^{(2)} (\langle |\mathbf{e}_{h,3}| \delta \mathbf{e}_{h,3}, \boldsymbol{\phi} \rangle + \langle |\delta \mathbf{e}_{h,3}| \mathbf{e}_{h,3}, \boldsymbol{\phi} \rangle) + \frac{\varepsilon_\omega}{k} \langle \delta \mathbf{e}_{h,3}, \boldsymbol{\phi} \rangle - \frac{\Gamma_0}{k v_t^2} \langle \delta \mathbf{a}_{h,3}, \boldsymbol{\phi} \rangle, \\ \mathcal{A}'_{h,n}{}^2(\mathbf{x})(\delta\mathbf{x}, \boldsymbol{\phi}) &= \varepsilon_\Delta \langle \delta \mathbf{e}_{h,2}, \boldsymbol{\phi} \rangle - \frac{k^2 v_t^2 - 12}{12 v_t^2} \langle \nabla \delta \mathbf{e}_{h,2}, \nabla \boldsymbol{\phi} \rangle + \frac{k \Gamma_0 + 6}{k v_t^2} \langle \delta \mathbf{a}_{h,2}, \boldsymbol{\phi} \rangle \\ &\quad - \frac{k \Gamma_0 + 6}{12 v_t^2} \langle \nabla \delta \mathbf{e}_{h,3}, \nabla \boldsymbol{\phi} \rangle - \frac{\varepsilon_\Delta (k \Gamma_0 + 6)}{12} \langle \delta \mathbf{e}_{h,3}, \boldsymbol{\phi} \rangle - \frac{k^2 v_t^2 + 6 k \Gamma_0 + 24}{12 k v_t^2} \langle \delta \mathbf{a}_{h,3}, \boldsymbol{\phi} \rangle, \\ \mathcal{A}'_{h,n}{}^3(\mathbf{x})(\delta\mathbf{x}, \boldsymbol{\phi}) &= \frac{k v_t^2 + 2 \Gamma_0}{2 v_t^2} \langle \nabla \delta \mathbf{e}_{h,2}, \nabla \boldsymbol{\phi} \rangle + \varepsilon_\Delta \Gamma_0 \langle \delta \mathbf{e}_{h,2}, \boldsymbol{\phi} \rangle + \frac{k^2 v_t^2 - 12}{k^2 v_t^2} \langle \delta \mathbf{a}_{h,2}, \boldsymbol{\phi} \rangle \\ &\quad + \frac{\varepsilon_\Delta}{k} \langle \delta \mathbf{e}_{h,3}, \boldsymbol{\phi} \rangle - \frac{k^2 v_t^2 - 12}{12 k v_t^2} \langle \nabla \delta \mathbf{e}_{h,3}, \nabla \boldsymbol{\phi} \rangle + \frac{k \Gamma_0 + 6}{k^2 v_t^2} \langle \delta \mathbf{a}_{h,3}, \boldsymbol{\phi} \rangle, \\ \mathcal{A}'_{h,n}{}^4(\mathbf{x})(\delta\mathbf{x}, \boldsymbol{\phi}) &= \frac{2 \varepsilon_\omega - k \varepsilon_\Delta \Gamma_0}{2} \langle \delta \mathbf{e}_{h,2}, \boldsymbol{\phi} \rangle - \frac{k \Gamma_0}{2 v_t^2} \langle \nabla \delta \mathbf{e}_{h,2}, \nabla \boldsymbol{\phi} \rangle - \frac{k v_t^2 + 2 \Gamma_0}{2 v_t^2} \langle \delta \mathbf{a}_{h,2}, \boldsymbol{\phi} \rangle + \frac{k}{12} \langle \delta \mathbf{a}_{h,3}, \boldsymbol{\phi} \rangle \\ &\quad + \chi^{(2)} (\langle |\delta \mathbf{e}_{h,2}| \mathbf{e}_{h,2} + |\mathbf{e}_{h,2}| \delta \mathbf{e}_{h,2}, \boldsymbol{\phi} \rangle) + \frac{k \Gamma_0}{12 v_t^2} (\langle \nabla \delta \mathbf{e}_{h,3}, \nabla \boldsymbol{\phi} \rangle + \langle \delta \mathbf{e}_{h,3}, \boldsymbol{\phi} \rangle). \end{aligned}$$

In every Newton step we have to solve a linear system of equations, for which we use the GMRES method with an algebraic multigrid solver, which serves as a preconditioner with a single sweep for every GMRES iteration. This accelerates the convergence of the GMRES iterations.

B. Extension of the neural operator to a full space-time approximation

We sketch how the solution operator U can be extended in order to obtain an approximation to \mathcal{S}_h . The idea is to construct an interpolation operator I_h which interpolates the solutions $\mathcal{U}^i(\mathbf{v})$ and $\mathcal{U}^{i+1}(\mathbf{v})$ in space. We need a finite-dimensional subspace $W \subset V$ of dimension $M = \dim(W)$. A standard example would be $W = V_h$, a classical finite element space, neural networks are feasible as well. First note that from Eq. (5.9) we see that $J_{D,i+1}$ is the set $J_{D,i}$, translated in positive x_1 -direction. For $i \in \{1, \dots, m\}$ we choose $x_a \in J_{D,i}$ and let $\mathcal{U}^{i-1}(g(t)) = \mathbf{p}(t, x_a)$. Then $U(\mathbf{p}(t, x_a)) = \hat{\mathbf{p}}(t, x_b)$ where $x_b \in J_{D,i+1}$. We choose a basis $\{\phi_1, \dots, \phi_J\}$ of W with support points J_D . Let ϕ_j^a denote basis functions with support points in $J_{D,i+1}$ and ϕ_j^b those with support points in $J_{D,i}$. On each subinterval I_n we can then interpolate

$$U|_{I_n}(x, t) = \sum_{k=0}^3 \xi_k(t) \left(\sum_{j=0}^{|J_{D,i}|} \mathbf{p}_k \phi_j^a(x) + \hat{\mathbf{p}}_k \phi_j^b(x) \right). \quad (\text{B.1})$$

Finally the solution operator $\mathcal{S}_h(g(t))$ can be approximated by recursive application of U to itself, i. e. $U \circ \dots \circ U(g(t)) =: \mathcal{U} \approx \mathcal{S}_h(g(t))$.

C. Physical Quantities and Quantites of Interest

We give some background on the quantities of interest in the simulations carried out in this work. To this end we first introduce the Poynting vector \mathbf{s} and optical power P (cf. [43, Chapter 6, Section 6]).

$$\mathbf{s} = \frac{1}{\mu_0} \mathbf{e} \times \mathbf{b}, \quad (\text{C.1}) \quad P = \int_A \mathbf{s} \cdot \mathbf{n} \, ds \quad (\text{C.2})$$

The flow of energy in an electromagnetic field, with the electric field \mathbf{e} and the magnetic field \mathbf{b} is described by the Poynting vector (C.1). The optical power P in (C.2) is the flux of the Poynting vector through a surface A . Then, the intensity is the magnitude of the Poynting vector and the average fluence is the mean of the intensity over time.

$$I_e = |\mathbf{s}| = \frac{P}{|A|}. \quad (\text{C.3}) \quad F = \frac{1}{T} \int_0^T I_e \, dt \quad (\text{C.4})$$

In the simplified 1D case, the optical intensity I_e and fluence F can be described by equations (6.6a) and (6.6b) respectively. We note that the intensity is proportional to the power and the fluence is proportional to the energy.